



## Research paper

## SphGLLTools: A toolbox for visualization of large seismic model files based on 3D spectral-element meshes

Caio Ciardelli <sup>a,b</sup>, Ebru Bozdağ <sup>b,\*</sup>, Daniel Peter <sup>c</sup>, Suzan van der Lee <sup>d</sup><sup>a</sup> Department of Geophysics, Institute of Astronomy, Geophysics and Atmospheric Sciences, University of São Paulo, Brazil<sup>b</sup> Department of Geophysics, Colorado School of Mines, United States of America<sup>c</sup> Division of Physical Sciences and Engineering, King Abdullah University of Science and Technology, Saudi Arabia<sup>d</sup> Department of Earth and Planetary Sciences, Northwestern University, United States of America

## ARTICLE INFO

## Keywords:

Computational seismology  
Full-waveform inversion  
Numerical wave propagation  
Seismic tomography  
Spectral-element method  
Spherical harmonics  
Visualization

## ABSTRACT

Adjoint tomography, a full-waveform inversion technique based on 3D wave simulations, has become a commonly used tool in passive-source seismology, drawing on advances in computational power and numerical methods. From global to reservoir scales, seismic models can iteratively be updated in adjoint inversions by extracting information from full seismic waveforms. Seismic models are typically constructed on the numerical mesh used for wave simulations. Thus the size of model files depends on the minimum resolvable period achieved in simulations controlled by the numerical mesh (the higher the mesh resolution, the larger the model and mesh files). This is specifically a concern for recent global-scale adjoint tomographic models where the size and format of numerical meshes pose challenges for model visualization, analysis, interpretation, and sharing model files. Here, we present SphGLLTools, an open-source toolbox that intends to diminish these challenges by expanding global adjoint models onto spherical harmonic functions, which are widely used in global seismology. Our tools are initially designed for spectral-element meshes used in recent global adjoint tomography studies. SphGLLTools facilitate many commonplace tasks for model visualization and analysis, including spherical harmonic expansion of models sampled on spectral-element meshes together with associated tools for easy sharing, visualization, and interpretation of large-scale seismic model files. All the developed routines are accompanied by user instructions and are available through [GitHub](https://github.com/bozdag/SphGLLTools). For transparency, reproducibility, and educational purposes, we also include [Colab notebooks](https://colab.research.google.com/github/bozdag/SphGLLTools), which provide an intuitive and comprehensive review of the principles and methods for spectral-element meshes, spherical harmonic expansion, and other model analysis tools.

## 1. Introduction

Imaging Earth's deep interior has been one of the major goals of geophysics. Seismic tomography is a powerful technique where seismologists use seismic waves generated by active or passive seismic sources (i.e., explosions, earthquakes, ambient noise, etc.) and recorded by seismic stations to infer Earth models for the spatial distribution of seismic parameters. Improving the resolution of these models is crucial for expanding insights into the inner structure, thermo-chemical composition, and geodynamical evolution of our planet.

Traditionally, seismic tomography is based on ray theory, a high-frequency approximation to describe wave propagation, which is valid when the dominant seismic wavelength is less than the scale length of

heterogeneities (Wang and Dahlen, 1995b; Spetzler et al., 2001). Ray theory has provided robust seismic models of Earth's interior within its validity regime, for instance, based on travel times of body waves, surface-wave phase and group velocities, normal-mode splitting functions, some S-wave and surface-wave waveforms, and the combination of all these data types to improve data coverage at the global scale (e.g., Chang et al., 2014; Ritsema et al., 1999, 2011; Kustowski et al., 2008; Moulik and Ekström, 2014). However, in the current resolution of seismic models finite-frequency effects have become important (Woodhouse and Girnius, 1982; Marquering et al., 1999) and have been taken into account in many global mantle models (e.g., Li and Romanowicz, 1996; Montelli et al., 2004).

\* Corresponding author.

E-mail addresses: [caio.ciardelli@alumni.usp.br](mailto:caio.ciardelli@alumni.usp.br) (C. Ciardelli), [bozdag@mines.edu](mailto:bozdag@mines.edu) (E. Bozdağ), [daniel.peter@kaust.edu.sa](mailto:daniel.peter@kaust.edu.sa) (D. Peter), [suzan@earth.northwestern.edu](mailto:suzan@earth.northwestern.edu) (S. van der Lee).URLs: <https://ebrucsm.wordpress.com/> (E. Bozdağ), <https://danielpeter.github.io/> (D. Peter), <http://geophysics.earth.northwestern.edu/seismology/suzan/> (S. van der Lee).

Ever-increasing computational power and advances in 3D numerical wave propagation solvers have made full-waveform inversion (FWI) feasible for large-scale passive-source tomography problems. First applications of FWI at the global scale combined full waveforms based on 3D spectral-element wave simulations with 2D asymptotic data sensitivity kernels (e.g., Lekić and Romanowicz, 2011; French and Romanowicz, 2014). The adjoint method (e.g., Plessix, 2006) allows for using 3D wave simulations in the computation of 3D data sensitivity kernels (Fréchet kernels). The theory was introduced to seismology by Tarantola (1984) where data sensitivity kernels of a chosen misfit function may be computed based on the interaction of (1) a forward wavefield, generated by a regular seismic source recorded by a regular seismic station, and (2) an adjoint wavefield, generated by a fictitious source based on the chosen misfit between data and synthetics at the location of the regular station and recorded by a fictitious station at the location of the regular seismic source (Tramp et al., 2005; Fichtner et al., 2006a,b). Hence, to compute 3D volumetric data sensitivity kernels, so-called adjoint kernels, and iteratively update seismic models, only two numerical simulations, one for forward and one for adjoint wavefields, are required (Tramp et al., 2005). There are now many applications of adjoint tomography in earthquake seismology at the crustal (e.g., Tape et al., 2009; Fichtner et al., 2013; Wang et al., 2018) and continental (e.g., Fichtner et al., 2009; Zhu et al., 2012; Chen et al., 2014; Zhu et al., 2015) scales. Finally, following the first demonstration by Afanasiev et al. (2016), first global adjoint models to image the whole Earth's mantle simultaneously inverted with the crust were published by Bozdag et al. (2016), Lei et al. (2020). The main advantage of FWI is the ability to extract more information from each waveform in seismic inversions by modeling the full complexity of wave propagation both in forward and adjoint wavefields based on 3D numerical simulations. Furthermore, the crust and mantle can simultaneously be updated in iterative inversions without the need for crustal corrections (Bozdag and Trampert, 2008; Ferreira et al., 2010; Bozdag et al., 2016).

FWI relies on high-accuracy seismic waveform simulations. The spectral-element method has been most efficient for simulating 3D wave propagation at the global scale due to its high-order accuracy of the full wavefield and in particular of surface waves, important for lateral coverage in global inversions (e.g., Komatitsch and Tromp, 1999; Chaljub et al., 2003; Capdeville et al., 2003; Komatitsch and Tromp, 2002a,b). The spectral-element method combines the flexibility of finite-elements to mesh complex structures together with a diagonal mass matrix which significantly reduces the cost of simulations and lends itself well to parallel computations on largest supercomputers. It has been further employed at crustal and continental scales (e.g., Tape et al., 2009; Zhu et al., 2012; Dong et al., 2021) as well as in industrial studies of FWI where different meshing strategies have been proposed to improve the resolution of numerical simulations (e.g., Trinh et al., 2017; Teodor et al., 2019; Pan et al., 2020). For instance, Araújo et al. (2021) managed to further optimize the spectral-element method by boosting memory access with Hilbert space-filling curves. There are also other efforts to address capturing complex structures efficiently in numerical simulations such as combining the finite-difference method with finite elements (e.g., Moczo et al., 2007; Gao and Keyes, 2019) and using meshless finite difference methods that do not require a predefined connection between nodes (e.g., Berljavac et al., 2021). The spectral-element method is a finite-element method that uses higher-order Lagrange basis functions in combination with so-called Gauss-Lobatto-Legendre (GLL) nodal points (Komatitsch and Vilotte, 1998; Komatitsch and Tromp, 1999). Numerical simulations are performed based on a mesh sampled at every GLL point. Spectral elements are a special kind of irregular grid where GLL points are defined based on a GLL basis and then mapped to the desired shape. Due to the chosen basis functions, the spectral-element method has the accuracy of pseudo-spectral methods and the flexibility of finite elements to mesh the computational domain (Komatitsch and Tromp,

2002a; Schubert, 2003). The distribution of GLL points allows for high accuracy and flexibility in simulations by solving the weak form of the wave equation using Gaussian quadrature (e.g., Komatitsch and Tromp, 1999; Schubert, 2003), a high-accuracy numerical integration method. The flexibility of spectral elements allows for accurately taking 3D variations in the crust, including topography, bathymetry. Spatially variable crustal thickness can be honored by the mesh to improve computational accuracy and efficiency, especially for surface waves sampling the oceanic crust, by stretching and distorting the spectral elements (Tromp et al., 2010). Homogenization of the crustal elastic properties could further be used in FWI applications to reduce computational costs (Capdeville and Marigo, 2007; French and Romanowicz, 2014; Fichtner et al., 2013).

In principle, the tomographic model discretization follows three main ideas: (1) adapt the parameterization to a priori information (e.g., finer discretization in the lithosphere, where we expect stronger heterogeneities than the rest of the model, increased spacing by depth, etc.), (2) adapt and optimize the mesh in the numerical solver (i.e., because of an increase in wavelengths by depth, element sizes in meshing might be increased) in case of numerical simulations, and (3) adapt to the data coverage in the inversion grid (i.e., address sparsity of data in inversions). Thus, one would have three different grids, and the problem lies in interpolating between them (Kissling et al., 2001). Generally, adaptive local grids (e.g., Zhou, 1996; Boschi and Dziewonski, 2000) or spherical harmonics (e.g., Li and Romanowicz, 1996; Ritsema et al., 1999; Boschi and Ekström, 2002; Lebedev et al., 2005) are used for horizontal parameterization with polynomials and splines in the vertical direction. The choice of parameterization is one of the factors that might control the resolution of tomographic models (e.g. Giardini et al., 1988; Snieder et al., 1991). Typically, FWI models are sampled on the mesh used for numerical simulations. The main advantage is that sensitivity kernels, models, and all the generated mesh files have the same spatial sampling so that models can be updated on the same mesh that is used for numerical simulations (Bozdag et al., 2016) during iterative inversions. The drawback is that as the mesh resolution increases, computational and storage requirements also increase. Alternative solutions for reducing file sizes include compression methods (Boehm et al., 2016) where the trade-off between the resolution and the size of the models should be taken into account.

Sampling model files on GLL points makes it impractical to visualize, investigate, and share models with other researchers because of their large sizes, especially at the global scale. The recent global adjoint models GLAD-M15 (Bozdag et al., 2016) and GLAD-M25 (Lei et al., 2020), for instance, are sampled by a mesh of ~4 million spectral elements with ~268 million GLL points leading to an accuracy of ~17 s minimum period in numerical simulations. Then the total size of the mesh and model files become ~47 GB. The size of the model and mesh files increases as the resolution of meshes increases to resolve shorter wavelengths, and parallel computing is needed to extract cross-sections at desired depths or great circles. A common way to share model files is to provide downsampled model parameters in ASCII or binary formats where the resolution can be degraded. More importantly, spectral-element simulations require the actual model files sampled on a specific mesh. Users need to interpolate and resample the original model files to the desired simulation resolution and partition spectral elements to different numbers of parallel processes. These complexities make the visualization and interpretation of models and numerical simulations at different resolutions impractical and time-consuming for users.

There is no consensus on model data formats to facilitate easy sharing between researchers. Various plotting engines and visualization tools are available in which seismic models are converted to a specific data format in a model library. For instance, IRIS (Incorporated Research Institutions for Seismology) usually provides seismic tomographic models in their original format or NetCDF format (network Common Data Form) on the EMC (Earth Model Collaboration) repository (Trabant et al., 2012; Hutko et al., 2017). EMC visualization

tools help to extract and visualize model data and metadata. Downsampled versions of the recent global adjoint tomography models (Bozdağ et al., 2016; Lei et al., 2020) are provided through IRIS to overcome the file size issue, reducing the model resolutions specifically in the lithosphere. Another example is the Oxford SubMachine (Hosseini et al., 2018), which is a collection of web-based tools for the interactive visualization, analysis, and quantitative comparison of global-scale, volumetric (3-D) data sets of the subsurface, with supporting tools for interacting with other, complementary models and data sets. Other tools, such as Postpischl et al. (2011) and Yamagishi et al. (2018) use the Keyhole Markup Language (KML) visualization layers (Burggraf, 2015) with the Google Earth geo-browser as a flexible platform that can substitute specialized graphical tools to perform qualitative visual data analyses and comparisons.

In this work, we provide a comprehensive set of routines for efficient visualization of large seismic models initially for global adjoint models based on spectral-element wave simulations. Strictly speaking, our tools are designed for the global adjoint tomography models GLAD-M15, GLAD-M25, and future models, which are constructed based on the spectral-element mesher of the open-source SPECFEM3D\_GLOBE package (Komatitsch and Tromp, 2002a,b). Our open-source toolbox, SphGLLTools, converts any spectral-element global model onto spherical harmonics expanded up to a requested degree (see Section 3 for further details about the expansion). Spherical harmonic expansion of spectral-element models drastically reduces the size of files, allowing for effective visualization and investigation of seismic models on a laptop and sharing them efficiently with other researchers. The toolbox also involves routines for creating block models (useful for parameterization of the crust), extracting and plotting horizontal & vertical cross-sections and one-dimensional profiles at desired locations, and computing global mean models in an efficient way based on spherical harmonic expansions. The output is saved as plain ASCII files, which are easily convertible to other formats (e.g., NetCDF) using external tools such as Python, GMT6 (Wessel et al., 2019), and QGIS (QGIS Development Team, 2009). In addition, we provide essential routines for spherical harmonic expansions, such as improved interpolation and smoothing tools that work on GLL meshes. SphGLLTools does not presume prior knowledge of particular numerical meshes or spherical harmonic functions. Users can go through each step and the pertinent theory by working through the accompanying Google Colab notebooks. Fourteen Colab notebooks provide interactive Python shells in which users can learn/review the theory and practice the algorithms by changing parameters, etc. The toolbox and the accompanying Colab notebooks are open source and have a manual that includes application examples. Although the software is originally designed for SPECFEM3D\_GLOBE meshes, it can be adapted to other numerical solvers in the future.

The manuscript is designed as follows: In Section 2 we give background information about spectral-element meshes and associated FWI models. After giving the theory of spherical harmonic expansion in Section 3.1 and showing how to combine them with B-splines to carry out volumetric expansion in Section 3.2.1, we describe how we expanded global adjoint models onto spherical harmonics by carefully accommodating crustal variations in Section 3.2.2. We present the main capabilities of SphGLLTools in Section 4 and an overall view of the toolbox in Section 5 followed by conclusions.

## 2. Global FWI models

In spectral-element simulations, seismic model parameters (i.e.,  $P$ - and  $S$ -wave velocities, density, attenuation, etc.) are sampled on a GLL mesh. In large-scale simulations, such as those performed for global adjoint tomography, the mesh is partitioned into many slices and distributed over multiple cores for parallel processing. These slices are typically stored as binary files or using modern data formats such as NetCDF (Unidata, 2016), HDF5 (Koranne, 2011) or ADIOS (Liu et al.,

2014). Unless model compression or some downsampling is applied, the files are sampled at every GLL point, leading to dozens of gigabytes of disk space depending on the model resolution. For instance, the minimum resolvable period of spectral-element simulations of the recent global adjoint tomography models (Bozdağ et al., 2016; Lei et al., 2020) is 17 s (NEX = 256, where NEX is the number of spectral elements at the surface on one side of each of six chunks of the globe), where the model size for a transversely isotropic parameterization is about 12 GB and 35 GB for model and mesh files, respectively. The size of the model and mesh files increases to about 78 GB and 230 GB, respectively, when the minimum resolvable period of global simulations goes down to ~9 s (NEX = 512).

One of the most common ways for visualization is performed by the visualization software Paraview (Ahrens et al., 2005) after combining all slices into a single VTU or VTK unstructured grid file or by using a parallel VTU (Schroeder et al., 2006) (PVTU) file format. Paraview allows for interactive 3D volumetric plots and the extraction of horizontal and vertical cross-sections. Sample cross-sections plotted by Paraview on a unit sphere are shown in Fig. 1. Creating VTU or VTK files before visualization requires direct access to the original mesh files, where generating them with the full resolution of the mesh may require parallel jobs to overcome the memory problems. Generally, for global adjoint models, VTU or VTK files are created using only the corner GLL points of each spectral element which may degrade the model resolution in plots, especially in the crust and upper mantle. Paraview provides an efficient way of plotting models in 3D. However, 2D cross-sections require additional steps, especially when we want to change the default projection.

For 2D depth slices and cross-sections, in seismology, it is common to use the GMT (Generic Mapping Tools) (Wessel et al., 2019) visualization package. To this end, depth slices at desired depths or vertical sections along desired paths must be extracted from model files. This process requires running parallel jobs with the mesh files and the number of processors used for numerical simulations. In this study, we expand global adjoint models sampled on spectral-element meshes onto spherical harmonics, which drastically reduces the model file size allowing for easy sharing, visualization, and investigation of global adjoint tomography models. Spherical harmonics are commonly used to horizontally parametrize ray-based global models together with splines in the radial direction (e.g., Ritsema et al., 1999, 2011; Chang et al., 2015). In our approach, we use spherical harmonic expansion horizontally and B-splines for vertical parameterization, as we describe below. For instance, the expansion of the mantle of GLAD-M15 (Bozdağ et al., 2016) onto spherical harmonics & B-splines (from the core-mantle boundary (CMB) to 80 km depth) occupies ~29 MB disk space only. For the mantle of GLAD-M25 (Lei et al., 2020), the size increases to ~55 MB since a higher-degree expansion is required to capture smaller-scale heterogeneities in the model adequately. To overcome the challenges of a spherical harmonic expansion due to the 3D crust, we store the top 80 km as a block model in binary format, which slightly decreases the advantage of our approach but increases the robustness of our analysis and visualization toolbox. A block model with a  $0.5^\circ \times 0.5^\circ$  horizontal and 1 km vertical resolution occupies ~537 MB and ~253 MB disk spaces for decompressed and compressed files, respectively, in the XZ-format, a high-ratio file compression based on the LZMA2 algorithm (Salomon, 2006).

## 3. Spherical harmonic expansion of global adjoint models

Spherical harmonics are useful for expanding functions defined on continuous surfaces with spherical symmetry. For low-frequency signals, a relatively small set of coefficients can accurately represent the entire function. Spherical harmonics also provide a concise way of analyzing the spectral content of data. We can think of them as a generalization of Fourier series (see the Colab notebook [Fourier series](#)) in combination with associated Legendre polynomials (see the Colab notebook [Associated Legendre polynomials](#)).

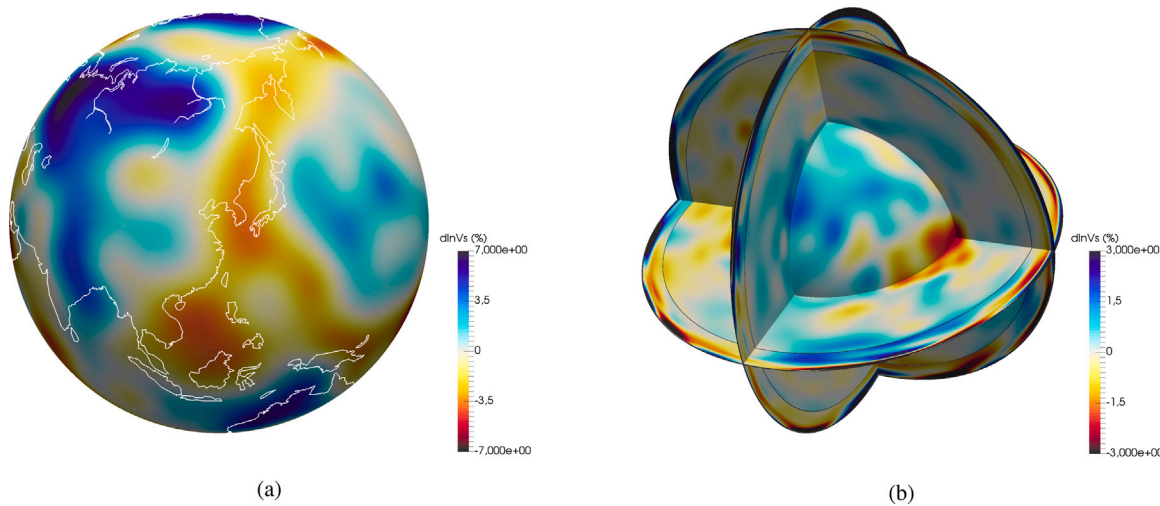


**Fig. 1.** Sample model visualization using Paraview (Ahrens et al., 2005). (a) Depth slice of shear-wave velocity perturbations of S362ANI (Kustowski et al., 2008) at 100 km. The velocity perturbations are computed with respect to the S362ANI's mean model (see Appendix). The white lines show continent boundaries. (b) Same as (a) but showing vertical cross-sections with a depth slice at the core-mantle boundary (CMB).

### 3.1. Spherical harmonics

Spherical harmonics are commonly used in global geophysical problems (e.g., Balmino et al., 1982; Carle and Harrison, 1982; Roithmayr, 2004; Schmidt et al., 2005). In seismology, some examples can be seen in ray-based seismic tomographic models (e.g., Ritsema et al., 1999, 2011; Chang et al., 2015). Here we use real spherical harmonics, as shown in Section B.8, Eq. B.99 of Dahlen and Tromp (1998). We begin by parametrizing the associated Legendre polynomials  $P_n^m$  in terms of  $\cos(\theta)$ , such that

$$P_n^m(\cos \theta) = \frac{(-1)^m}{2^n n!} (\sin \theta)^m \left[ \frac{d}{d(\cos \theta)} \right]^{n+m} (\cos^2 \theta - 1)^n \quad (1)$$

$$0 \leq m \leq n \quad m, n \in \mathbb{N},$$

where  $\theta$  is the colatitude and  $\cos(\theta)$  changes over  $[0, \pi]$ . We define  $X_{n,m}(\cos \theta)$  as the normalized version of  $P_n^m(\cos \theta)$  in the following form:

$$X_{n,m}(\cos \theta) = \sqrt{(2 - \delta_m^0) \frac{(2n + 1)}{4\pi} \frac{(n - m)!}{(n + m)!}} P_n^m(\cos \theta), \quad (2)$$

where  $\delta_m^0$  is the Kronecker delta

$$\delta_m^0 = \begin{cases} 1 & \text{if } m = 0 \\ 0 & \text{otherwise.} \end{cases} \quad (3)$$

We can then expand a spherically symmetric function  $f(\theta, \phi)$ , where  $\phi$  is the longitude, onto spherical harmonics such that

$$f(\theta, \phi) = \sum_{n=0}^{\infty} \sum_{m=0}^n (a_{m,n} \cos m\phi + b_{m,n} \sin m\phi) X_{n,m}(\cos \theta), \quad (4)$$

where

$$\begin{aligned} a_{m,n} &= \int_{-\pi}^{\pi} \int_0^{\pi} f(\theta, \phi) X_{n,m}(\cos \theta) \cos m\phi \sin \theta d\theta d\phi, \\ b_{m,n} &= \int_{-\pi}^{\pi} \int_0^{\pi} f(\theta, \phi) X_{n,m}(\cos \theta) \sin m\phi \sin \theta d\theta d\phi. \end{aligned} \quad (5)$$

The reader is referred to the Colab notebooks for more details about spherical harmonics.

### 3.2. Volumetric expansion

Many global seismic models use spherical harmonics as basis functions. For instance, 3D global mantle models S362ANI (Kustowski et al., 2008) and S362D1 (Gu et al., 2001) use spherical splines (Wang and

Dahlen, 1995a) to parametrize lateral velocity variations and cubic B-splines for radial parameterization. Splines are piecewise polynomial curves that are differentiable up to a specific order (Prautzsch et al., 2002). The degree  $n = 1$  spline, for example, is a set of linear segments connecting the points to be interpolated. The so-called natural cubic splines ( $n = 3$ ) are commonly used for fourth-order accuracy in interpolation, having  $C2$  continuity (i.e., continuity up to the second derivative) between successive interpolation points and achieving minimum oscillation (Ahlberg et al., 1967). Spline functions may be represented by a linear combination of basis functions known as B-splines (see Section 3.2.1).

Spherical harmonics were introduced into global mantle tomography by Dziewonski et al. (1977), in which the parameterization consists of a set of spherical shells where each shell was independently expanded onto spherical harmonics. Models S20RTS (Ritsema et al., 1999) and S40RTS (Ritsema et al., 2011) are parametrized horizontally in terms of spherical harmonics up to degrees  $N_{max} = 20$  and  $N_{max} = 40$ , respectively, and radially with a set of 21 cubic splines. S20A (Ekström and Dziewonski, 1998) uses spherical harmonics up to degree  $N_{max} = 20$  horizontally, and the upper and the lower mantles are parametrized separately by two sets of Chebyshev polynomials in the radial direction. SAW24B16 (Mégnin and Romanowicz, 2000) is parametrized by spherical harmonics up to degree  $N_{max} = 24$  to capture lateral velocity variations and 16 B-splines in the radial direction. Our choice to expand the global adjoint models GLAD-M15 (Bozdag et al., 2016) and GLAD-M25 (Lei et al., 2020) is similar to that of Mégnin and Romanowicz (2000) which combines spherical harmonics over  $\theta, \phi$  with cubic B-spline functions as a function of radius. In our case, we use 25 B-splines (Fig. 2).

#### 3.2.1. B-splines & spherical harmonics

Using B-splines, a spline function  $S$  as a function of radius  $r$  may be represented by a linear combination of  $n$ -degree basis functions  $B_{k,n}(r)$  over  $N_k$  control points, such as

$$S(r) = \sum_{k=0}^{N_k} c_k B_{k,n}(r), \quad (6)$$

where  $c_k$  are the coefficients of the expansion given as (see also the Colab notebook B-splines)

$$c_k = A_{k,k'}^{-1} \int_{t_0}^{t_{N_k}} f(x) B_{k',n}(r) dr, \quad (7)$$

$$A_{k,k'} = \int_{t_0}^{t_{N_k}} B_{k,n}(r) B_{k',n}(r) dr. \quad (8)$$

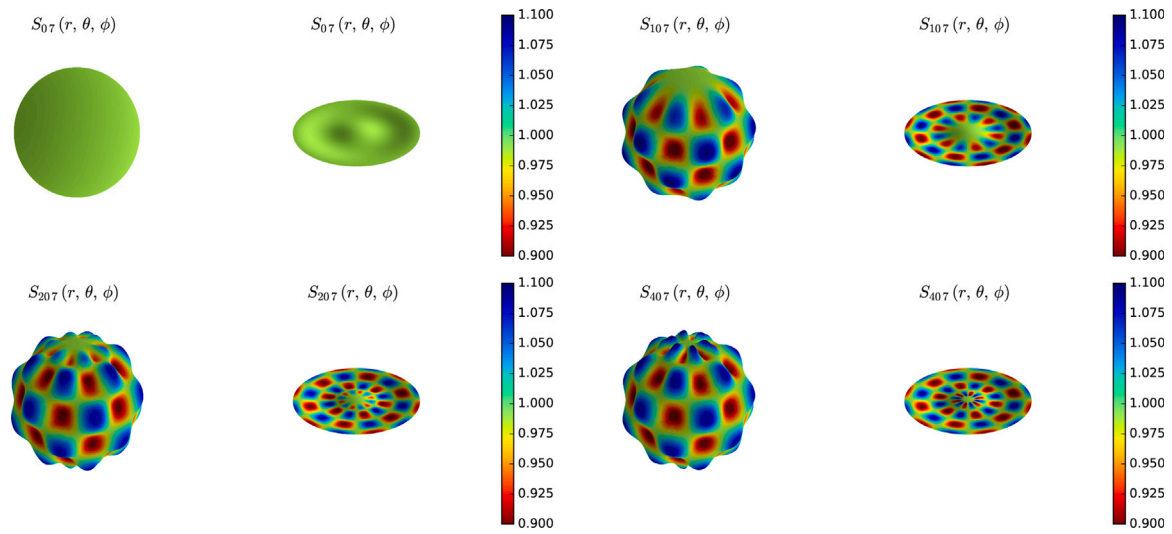


**Fig. 2.** Example of volumetric expansion  $S_{n,7}(r, \theta, \phi)$  using eight cubic B-splines for degrees 0 (upper-left corner), 10 (upper-right corner), 20 (lower-left corner) and 40 (lower-right corner) of  $f(r, \theta, \phi)$ . On the left of each subfigure, we show the surface of the expansion. A depth slice of its interior appears on the right.

We can approximate a function  $f(r, \theta, \phi)$  by combining B-splines and spherical harmonics, such as

$$f(r, \theta, \phi) \approx \sum_{s=0}^{N_s} \sum_{n=0}^{\infty} \sum_{m=0}^n R_s(r) (a_{m,n,s} \cos m\phi + b_{m,n,s} \sin m\phi) X_{n,m}(\cos \theta), \quad (9)$$

where the coefficients  $a_{m,n,s}$  and  $b_{m,n,s}$  are given as

$$\begin{aligned} a_{m,n,s} &= \sum_{s'=0}^{N_s} A_{s',s}^{-1} \int_{-\pi}^{\pi} \int_0^{\pi} \int_{r_1}^{r_2} R_s(r) f(r, \theta, \phi) X_{n,m}(\cos \theta) \\ &\quad \times \cos m\phi r^2 \sin \theta dr d\theta d\phi, \\ b_{m,n,s} &= \sum_{s'=0}^{N_s} A_{s',s}^{-1} \int_{-\pi}^{\pi} \int_0^{\pi} \int_{r_1}^{r_2} R_s(r) f(r, \theta, \phi) X_{n,m}(\cos \theta) \\ &\quad \times \sin m\phi r^2 \sin \theta dr d\theta d\phi. \end{aligned} \quad (10)$$

In Eq. (10),  $R_s(r) = B_{s,3}(r)$  is the radial basis composed of cubic B-splines where  $A_{s',s}$  is given as

$$A_{s',s} = \int_{t_0}^{t_{N_s}} B_{s',n}(r) B_{s,n}(r) r^2 dr. \quad (11)$$

Fig. 2 shows an example for a test function given by the following equation (see the Colab notebook [Volumetric expansion](#))

$$f(r, \theta, \phi) = \cos(2\pi r) \left( 1 + \frac{\sin 6\theta \sin 6\phi}{10} \right), \quad (12)$$

where  $r$ ,  $\theta$  and  $\phi$  are defined over  $0 \leq r \leq 1$ ,  $0 \leq \theta \leq \pi$  and  $-\pi \leq \phi \leq \pi$ , respectively.

The ideal maximum degree of the expansion,  $N_{max}$ , may vary by depth since we have different scale lengths of heterogeneities, for instance, in the upper mantle, lower mantle, and the D'' region. However, a single basis function may span hundreds of kilometers in the radial direction (Fig. 3). Therefore, one must cautiously determine the ideal degree of expansion since a higher spherical harmonic degree than the one required to capture the scale-length of heterogeneities may introduce artificial numerical noise into the expansion. On the other hand, regardless of the chosen expansion method, spherical harmonics can be thought of as a kind of data compression technique where we may lose some short-wavelength information while reducing the model size.

### 3.2.2. Expansion of global adjoint models

Spectral-element meshes in the SPECFEM3D\_GLOBE package consist of three major zones: crust & mantle, fluid outer core, and the solid inner core. A global mesh consists of six chunks surrounding a cube

of spectral elements at the center of the planet where the central cube avoids the singularity at the origin of the spherical coordinate system (Chaljub, 2000). The size of spectral elements is doubled once below the crust-mantle boundary (Mohorovičić or Moho discontinuity), a second time below the 650 km discontinuity, and a third time just above the inner core boundary (ICB) (Komatitsch and Tromp, 2002a) to optimize the cost of global wave simulations. For 3D global models, the mesh honors internal first-order discontinuities of the corresponding 1D reference model, e.g., PREM (Dziewonski and Anderson, 1981), and 3D crustal thickness variations for better accuracy of numerical simulations by a denser sampling of specifically the thin oceanic crust (Tromp et al., 2010).

B-splines and spherical harmonics cannot directly handle sharp first-order discontinuities in the mesh (i.e., the Moho and upper-mantle discontinuities, the CMB). As expected, the most challenging one is the Moho discontinuity, which dramatically affects seismic wave propagation, specifically of surface waves. During the construction of the recent global adjoint models, the crust and mantle were inverted simultaneously (e.g., Bozdağ et al., 2016). The Moho discontinuity can vary in depth from 7 km underneath oceans up to 70 km underneath continents (i.e., Himalayas, Andes) (e.g., Bassin et al., 2000; Laske et al., 2012) which causes significant oscillations in the spherical harmonic expansion. To avoid numerical instabilities, we prefer to represent the top 80 km of the Earth as a block model. The rest of the mantle is split into three distinct mantle regions (the upper mantle, the transition zone, and the lower mantle) and parametrized by a volumetric expansion using B-splines and spherical harmonics. For this study, we ignore the fluid outer core and the solid inner core as current adjoint models only update the crust and mantle.

To create the block model for the top 80 km, we first switch off the Earth's ellipticity in the mesh by slightly stretching all spectral elements. Then, we use interpolation to sample the mesh on a regular grid from 80 km depth (the bottom of the second layer of spectral elements) to the desired elevation (e.g., 5 km above the sea level). We then create the block model at any desired resolution. For instance, for the top 80 km of GLAD-M15 and GLAD-M25 we use a resolution of  $0.5^\circ \times 0.5^\circ$  and 1 km horizontally and vertically, respectively. Once we have the block model, we need an accurate interpolation scheme for visualization and any other processes such as sampling the block model with the spectral-element mesh when needed. We use trilinear interpolation, which does not suffer from the Gibbs phenomenon at the discontinuities present within the crust.

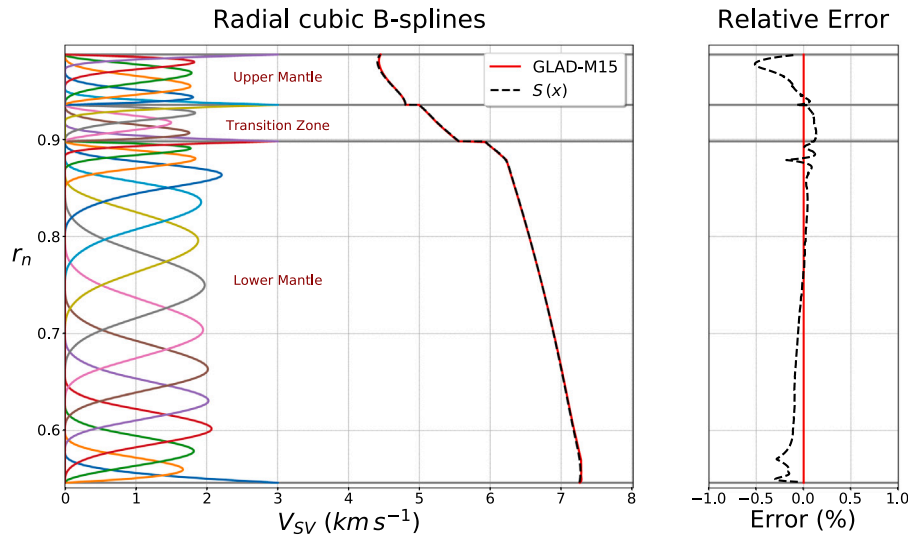


**Fig. 3.** Left: Twenty-five cubic B-splines used in the radial direction in the GLAD-M15 expansion. The number and distribution of the B-splines within the upper mantle, transition zone, and lower mantle are fine-tuned to achieve maximum accuracy. The mean  $V_{SV}$  as a function of depth (red line) and the reconstruction of the model from the B-splines  $S(x)$  and the coefficients (black dashed line) are shown on the right of the figure. Right: Relative error between  $S(x)$  and the mean  $V_{SV}$ . The error is larger in regions with strong heterogeneity (i.e., the uppermost mantle (~0.5%) and the D'' layer (~0.25%)), and smaller in a less heterogeneous region (i.e., the lower mantle (<0.1%)).

For the rest of the mantle, instead of using a single set of cubic B-splines to represent the whole model, we split the mantle into three regions (the upper mantle, the transition zone, and the lower mantle) and expand them onto spherical harmonics separately. We use 14 B-splines in the lower mantle, 5 in the transition zone, and 6 in the upper mantle (Fig. 3). We remove the topographic variations on the upper-mantle discontinuities (i.e., 410 and 650 km) in the mesh by stretching spectral elements to obtain fully spherical interfaces. This procedure avoids interpolating mantle velocities across discontinuities and, therefore, aliasing in the spherical harmonic expansions. It is also more convenient for visualization to avoid sampling the upper mantle and transition zone or the transition zone and lower mantle grid points at a depth slice taken near one of these discontinuities.

In Section 3.2.1, we present the expressions to expand a generic function  $f(r, \theta, \phi)$  defined on an arbitrary grid using a combination of B-splines and spherical harmonics. In the GLL mesh, integration is performed using Gaussian quadrature (see the Colab notebook [Gaussian quadrature](#)), an accurate numerical integration method (see the Colab notebook on [Numerical methods](#)). Therefore, the expressions for calculating the spherical harmonic coefficients of model parameters defined on the GLL mesh (see the complete derivation in the Appendix B of [Lei et al. \(2020\)](#)) becomes

$$a_{m,n,s} = \sum_{s=0}^{N_s} A_{s',s}^{-1} \sum_{\text{elem } \alpha, \beta, \gamma} \omega_\alpha \omega_\beta \omega_\gamma R_s(r) f'(r, \theta, \phi) J^{\alpha, \beta, \gamma} \times X_{n,m}(\cos \theta) \cos m\phi, \quad (13)$$

$$b_{m,n,s} = \sum_{s=0}^{N_s} A_{s',s}^{-1} \sum_{\text{elem } \alpha, \beta, \gamma} \omega_\alpha \omega_\beta \omega_\gamma R_s(r) f'(r, \theta, \phi) J^{\alpha, \beta, \gamma} \times X_{n,m}(\cos \theta) \sin m\phi,$$

where  $f'(r, \theta, \phi)$  is a discontinuous function representing the Earth's model parameters to be expanded,  $\omega_\alpha$ ,  $\omega_\beta$  and  $\omega_\gamma$  are the GLL weights and  $J^{\alpha, \beta, \gamma}$  is the Jacobian.

Fig. 3 shows the setup for the radial B-splines of the three distinct mantle regions and the 1D mean depth profile for the expansion of GLAD-M15. Combining a block parameterization for the uppermost mantle and the crust and the spherical harmonic expansions for the rest of the mantle, we achieve less than 0.1% error in the crust, except around the Moho of thick crustal regions (e.g., the Andes and

Himalayas), where the error can be as large as 0.5%. Note that classical ray-based global mantle models do not suffer from this problem since they generally involve crustal corrections and start from 24 km depth (e.g., [Ritsema et al., 1999, 2011](#); [Kustowski et al., 2008](#)).

One of the advantages of carrying out independent expansions for the upper mantle, the transition zone, and the lower mantle is that we can use different degrees of spherical harmonics in each region, depending on the required resolution to capture the scale-length of heterogeneities. In GLAD-M15, for example, when expanding vertically-polarized shear-wave velocities ( $V_{SV}$ ), we use degree  $N_{max} = 100$  for the upper mantle to fully capture the resolution of the GLL model. However, for the transition zone and the lower mantle, lower degrees of spherical harmonic expansions  $N_{max} = 90$  and  $N_{max} = 80$ , respectively, are enough. For GLAD-M25, we use degrees  $N_{max} = 155$ ,  $N_{max} = 144$ ,  $N_{max} = 95$  in the upper mantle, the transition zone, and the lower mantle, respectively. These values are determined by trial and error until the difference between the GLL model and its spherical harmonics version is minimum. Reducing the maximum degree in the transition zone and the lower mantle speeds up expansions. Furthermore, it also avoids spurious oscillations in the deeper parts of the model, which may happen when a higher degree expansion than needed is used.

The spherical harmonic expansion of global adjoint models with a block model on top also facilitates their implementation into SPECFEM3D\_GLOBE, similar to other default global models in the package such as S40RTS ([Ritsema et al., 2011](#)) and S362ANI ([Kustowski et al., 2008](#)). This would allow users to change the resolution of simulations and partition of spectral elements for parallel computing without the need for interpolating meshes. For numerical seismic wave simulations, one can then turn on the surface and internal topographies and Earth's ellipticity. The relative errors of the current spherical harmonics and block parameterizations compared to the original GLL model (Fig. 3) may affect numerical global wave simulations. Implementation of the spherical harmonic expansion of global adjoint models into SPECFEM3D\_GLOBE is part of future studies. We focus on the visualization of these large-scale seismic models in this manuscript.

#### 4. Visualization

In addition to expanding spectral-element models onto spherical harmonics at desired degrees, SphGLLTools provides optimized C and Python routines for multiple tasks, such as extracting horizontal and

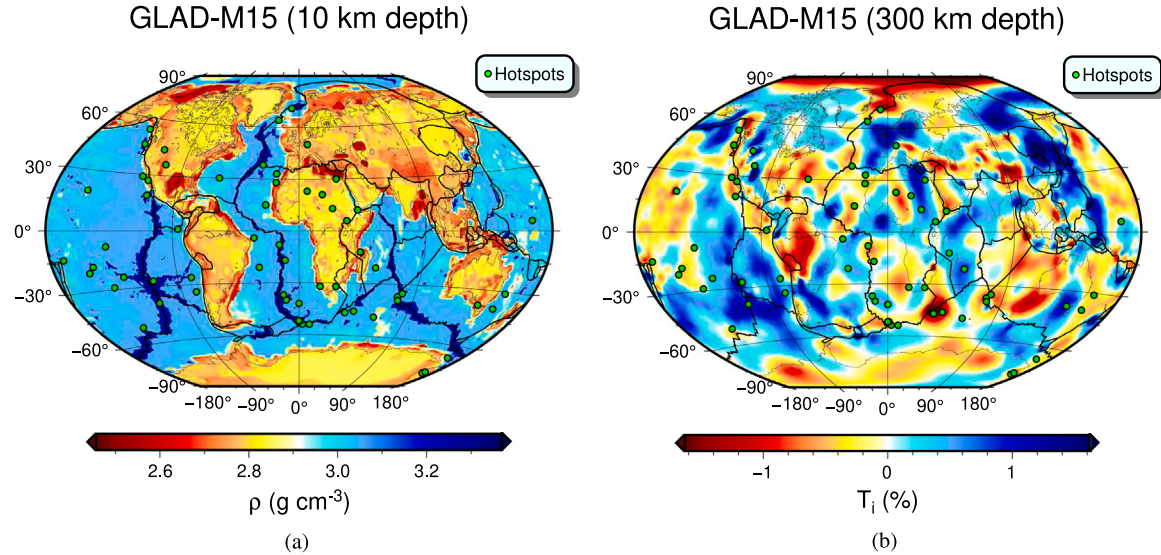


**Fig. 4.** (a) Depth slice of density from GLAD-M15 (Bozdağ et al., 2016) at 10 km depth. The green dots represent the hot spots compiled by Don L. Anderson using a large number of sources, and the black lines denote the plate boundaries DeMets et al. (2010). (b) Transverse isotropy (logarithmic ratio between  $V_{SV}$  and  $V_{SH}$ ) of GLAD-M15 at 300 km depth.

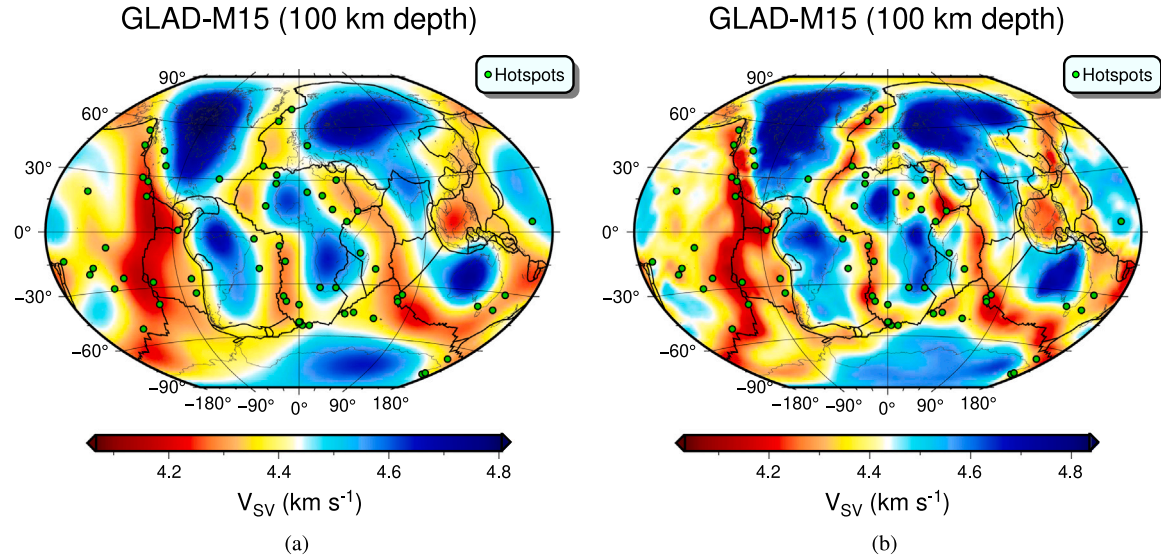


**Fig. 5.** (a) Depth slice of vertically-polarized shear-wave velocities ( $V_{SV}$ ) from GLAD-M15 at 100 km depth expanded up to degree 10. (b) Same as (a), but for spherical harmonic expansion up to degree 100.

vertical cross-sections, one-dimensional profiles at desired points on the surface, and computing power spectra of models. The package also has routines that can read the complex GLL mesh structure, interpolate it for spherical harmonic expansions, and take cross-sections directly from the spectral-element mesh in ASCII format, which requires parallel jobs. The routines can also calculate model perturbations with respect to the global mean of a chosen parameter (see [Appendix](#)). The toolbox includes Python scripts to compute additional parameters such as the bulk sound speed, transverse isotropy,  $V_p$  to  $V_s$  ratio, isotropic velocities, etc. In addition, we provide a set of Shell scripts for plotting, written in GMT6. [Figs. 4](#) and [5](#) show examples of such depth slices.

A great benefit of using spherical harmonics is that we can create cross-sections from the expansion with much less effort than using interpolation of the original GLL models. There is no need for parallelization, large memory, or storage. Any personal computer can be used to visualize or compute additional parameters in a few minutes or seconds, depending on the maximum degree of the expansion. The models can easily be analyzed at different spherical harmonics

degrees ([Fig. 5](#)). [Fig. 6](#) shows sample vertical cross-sections plotted by the toolbox for absolute values and perturbations of SV velocities of GLAD-M15, while one-dimensional sample profiles of the absolute SV velocities and their perturbations as a function of radius are presented in [Fig. 7](#).

In [Fig. 8](#), we illustrate the error introduced into models due to the block model at 50 km depth where the error is less than  $\sim 0.1\%$ , and spherical harmonic expansions at 110 km and 1600 km where we observe the maximum  $\sim 0.5\%$  and minimum  $\sim 0.06\%$  errors (see also [Fig. 3](#)). These errors are negligible from the model visualization point of view and model interpretation. However, it should be noted that they may significantly affect global surface wave propagation in case the expanded models are used in numerical simulations.

#### 4.1. Power spectra

Power spectra are useful for analyzing the spectral content of tomographic models (Chevrot et al., 1998). Following Eq. B.104 in Section

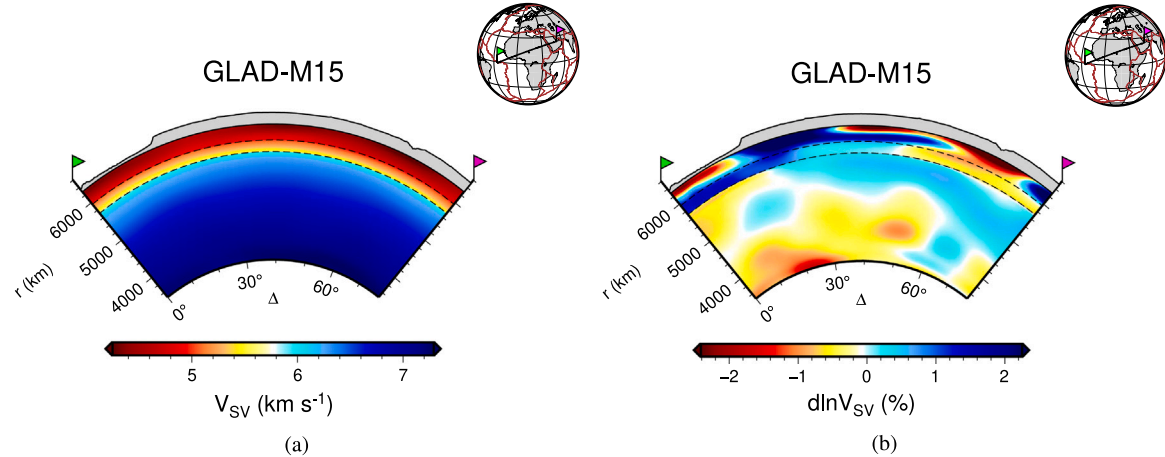


**Fig. 6.** (a) Vertical cross-section of vertically polarized shear-wave velocities ( $V_{SV}$ ) from GLAD-M15 along a great circle path (the black line connecting the flags in the inset map) from the CMB up to 80 km depth. (b) Same as (a), but showing model perturbations instead of the absolute values. In both figures, we expanded the model up to the maximum degrees in each zone: 100 for the upper mantle, 90 for the transition zone, and 80 for the lower mantle.

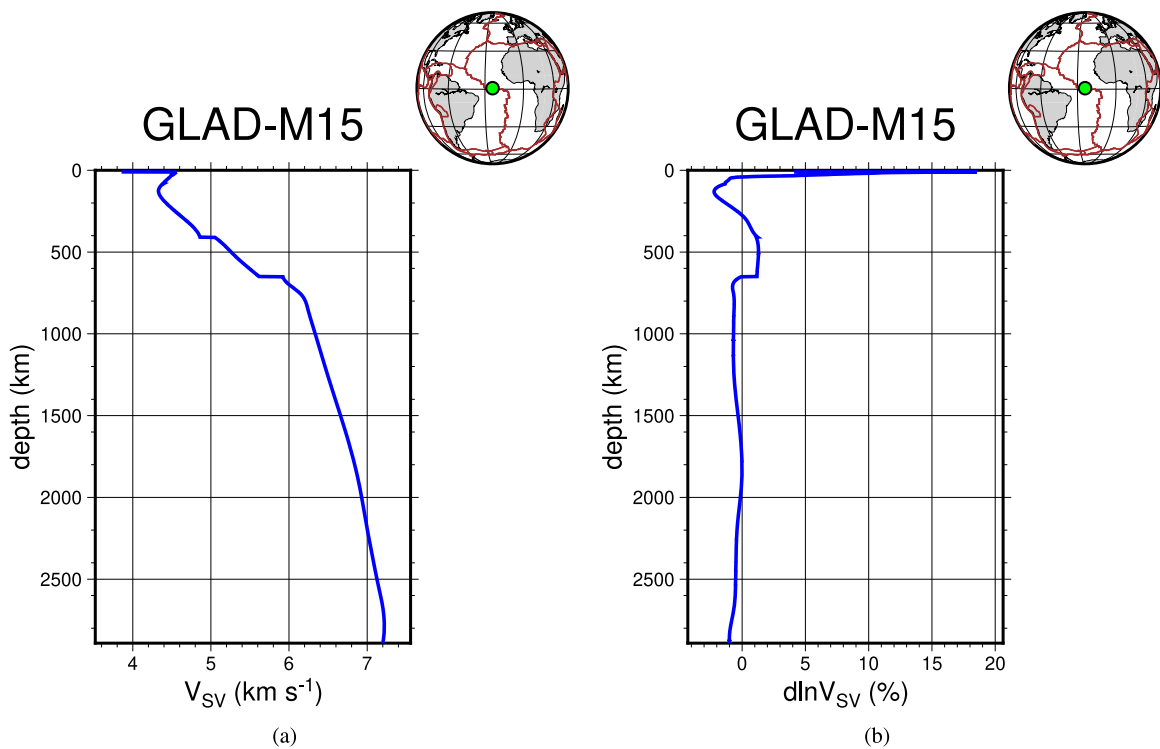


**Fig. 7.** (a) One-dimensional profile of vertically-polarized shear-wave velocities ( $V_{SV}$ ) from GLAD-M15 at a given location (green point in the inset map) from the CMB up to 10 km depth. (b) Same as (a), but model perturbations instead of absolute values. In both figures, we expanded the model up to degree 40.

B.8 of Dahlen and Tromp (1998) and Eqs. B.9 & B.10 in the appendix of Lei et al. (2020), we compute the normalized power per degree  $\sigma_n^2$  as

$$\sigma_n^2 = \frac{1}{2n+1} \sum_{s=0}^{N_s} \sum_{s'=0}^{N_s} A_{s,s'} \sum_{m=0}^n (a_{m,n,s} a_{m,n,s'} + b_{m,n,s} b_{m,n,s'}) , \quad (14)$$

and the normalized power per degree as a function of radius  $\Sigma_n^2(r)$  is determined as

$$\Sigma_n^2(r) = \frac{1}{2n+1} \sum_{s=0}^{N_s} \sum_{s'=0}^{N_s} R_s(r) R_{s'}(r) \times \sum_{m=0}^n (a_{m,n,s} a_{m,n,s'} + b_{m,n,s} b_{m,n,s'}) . \quad (15)$$

**Fig. 9** shows sample power spectra computed for S40RTS (Ritsema et al., 2011) and GLAD-M25 (Lei et al., 2020) up to spherical harmonics degrees  $N_{max} = 40$  and  $N_{max} = 60$ , respectively. S40RTS is a ray-based isotropic shear-wave velocity model constructed based on body-wave travel times, normal-mode splitting functions, and surface-wave dispersion data. GLAD-M25 is a global adjoint model which is the result of 10 more L-BFGS iterations after GLAD-M15 (Lei et al., 2020) where the power spectra show the smaller-scale heterogeneity content of GLAD-M25 up to degree  $N_{max} = 60$  in the upper mantle down to about 1200 km depth.

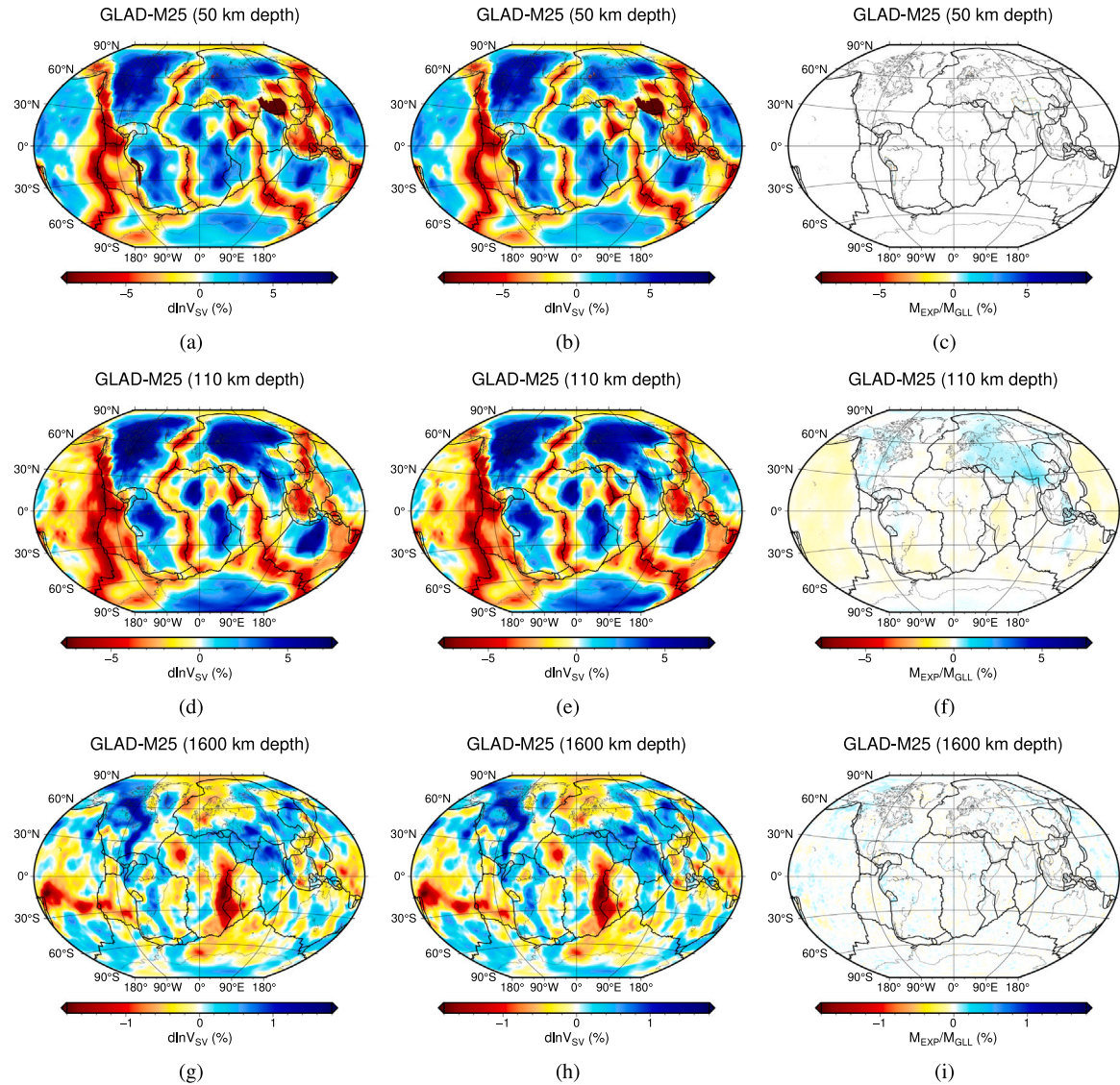


**Fig. 8.** Illustration of the error introduced by the spherical harmonic expansion of GLAD-M25 (Lei et al., 2020) at 50 km depth (crust), 110 km depth (where the error in the mantle is maximum), and 1600 km depth (where the error in the mantle is minimum). (a), (d) & (g) Shear-wave velocities of GLAD-M25 sampled on the spectral-element mesh at 50 km, 110 km, and 1600 km depths. (b), (e) & (h) Same as (a), (d) & (g) but for GLAD-M25 expanded onto spherical harmonics. (c), (f) & (i) Error between the GLL version of GLAD-M25 and its expansion at 50 km, 110 km, and 1600 km depths. In the crust 8(c), the error is usually less than 0.1%, except around the Moho of thick crustal regions (e.g., the Andes and Himalayas), where it can be as large as 0.5%. In the mantle, the maximum errors are slightly lower than 0.5% and around 0.06% at 110 km and 1600 km, respectively (see Fig. 3).

## 5. Overall view of the toolbox

SphGLLTools has additional routines to prepare GLL models for spherical harmonic expansions such as the Gaussian smoothing (Section 5.1) and interpolation (Section 5.2). Smoothing and interpolation routines are also commonly used in the global adjoint tomography workflow, for instance, to process the computed gradient and change the mesh or the number of the compute nodes, respectively. We explain the theory behind these algorithms for educational purposes and ensuring reproducibility. As previously mentioned, before expanding a spectral-element model onto spherical harmonics, one needs to remesh it on a spherically symmetric mesh using interpolation. Interpolation is also needed to create a block model to represent the top 80 km of global models. In addition to SphGLLTools visualization capabilities based on spherical harmonic models, the toolbox also includes routines to take horizontal and vertical cross-sections directly from spectral-element meshes based on a high-accuracy interpolation scheme we developed. These routines also assist spherical harmonic expansions to check their

accuracy where taken cross-sections and 1D profiles can directly be compared to those from the GLL models.

### 5.1. Gaussian smoothing in a GLL mesh

One can apply Gaussian smoothing to any grid type, including a GLL mesh. Usually, it is essential to smooth the numerically computed gradient based on a chosen misfit function to remove the numerical noise in the form of high-frequency artifacts (Komatitsch et al., 2016; Bozdag et al., 2016). On the other hand, smoothing can also be applied to spectral-element models before interpolation, if needed, to avoid potential numerical artifacts, which may also be useful to prevent aliasing when interpolating to lower-resolution meshes. The Gaussian smoothing is performed via convolution of the input model with a Gaussian function  $G_{\sigma_h, \sigma_v}$  (Eq. (17)), where  $\sigma_h$  and  $\sigma_v$  are the half-widths (semi-axis) of the Gaussian spheroid (ellipsoid of revolution) in the horizontal and vertical directions  $h$  and  $v$ , respectively (see the Colab

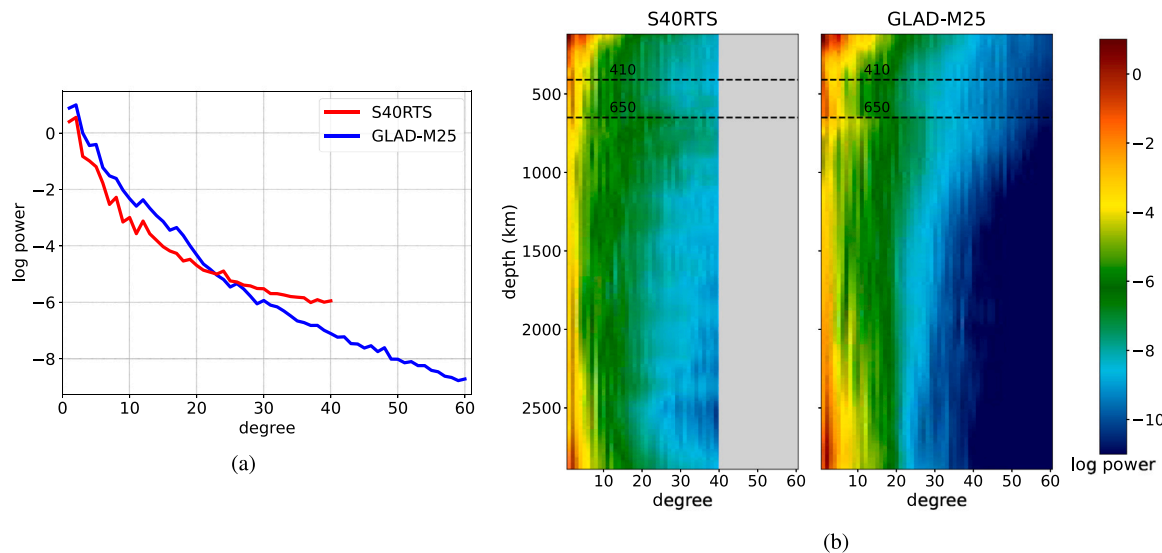


**Fig. 9.** (a) Normalized power per degree of vertically-polarized shear-wave velocities ( $V_{SV}$ ) for S40RTS (red) and GLAD-M25 (blue). (b) Normalized power per degree as a function of depth of  $V_{SV}$  for S40RTS (left) and GLAD-M25 (right).

**Table 1**

Smoothing profiles. The first column contains the depth of the top of each layer.  $\sigma_{h1}$  is the horizontal smoothing (half-width of the Gaussian kernel in the horizontal direction, i.e., the horizontal standard deviation) and  $\sigma_{v1}$  is the vertical smoothing (half-width in the vertical direction, i.e., the vertical standard deviation).

Depth (km)	$\sigma_{h1}$	$\sigma_{v1}$	$\sigma_{h2}$	$\sigma_{v2}$	$\sigma_{h3}$	$\sigma_{v3}$
-10	5	5	50	5	100	5
100	10	10	50	10	100	10
200	20	20	50	20	100	20
300	30	30	50	30	100	30
410	40	40	50	40	110	40
520	50	50	50	50	120	50
650	60	60	60	60	130	60
1000	70	70	70	70	140	80
2000	80	80	80	80	150	100

notebook on [Gaussian smoothing](#) for further details), such that

$$G_{\sigma_h, \sigma_v}(h, v) = \frac{e^{-\frac{1}{2} \left( \frac{h^2}{\sigma_h^2} + \frac{v^2}{\sigma_v^2} \right)}}{N}, \quad (16)$$

where

$$N = \int_{-\infty}^{\infty} \int_{-\infty}^{\infty} e^{-\frac{1}{2} \left( \frac{h^2}{\sigma_h^2} + \frac{v^2}{\sigma_v^2} \right)} dh dv. \quad (17)$$

The Gaussian smoothing routine can use different filters at each depth adapted according to the scale-length of heterogeneities in horizontal and vertical directions. The algorithm ensures a smooth transition from one filter to another, thereby preventing numerical artifacts. It can also preserve internal discontinuities if desired (Fig. 10).

## 5.2. Spectral-element interpolation

Interpolation is often needed to change the mesh resolution and the number of parallel processes in spectral-element simulations. For performance reasons, SPECFEM3D\_GLOBE partitions the mesh into many slices, one for each parallel process. The user chooses the number of slices and the mesh resolution when creating the mesh. However, once the mesh files are created, simulations must be run with the same number of cores and mesh resolution. Spectral-element models must be remeshed to change the number of cores for parallel numerical simulations or the resolution of a mesh. This is accomplished by interpolating the original mesh to re-partition and resample it onto the desired mesh

resolution. Interpolation is also often needed to extract horizontal and vertical cross-sections and 1D mean profiles of parameters directly from the spectral-element mesh.

The spectral-element method uses Lagrange interpolation (see the Colab notebook [Lagrange interpolation](#)), which can also be used for our purposes. As explained below, using Lagrange interpolation requires finding which spectral element encloses the point we want to interpolate. Nevertheless, since the elements are usually distorted and rotated (Fig. 11), figuring out which element contains each point becomes challenging. That requires fitting polynomial surfaces to each face of all elements, which is accomplished using a combination of multiple interpolation schemes in one, two, and three dimensions.

One of the main advantages of using finite elements is that the GLL mesh can deform to accommodate lateral variations in the Earth model. Although each element has a unique shape, position, and orientation, they can all be mapped to the canonical basis  $-1 \leq \xi \leq 1$ ,  $-1 \leq \eta \leq 1$  and  $-1 \leq \gamma \leq 1$  (where  $\xi$ ,  $\eta$ , and  $\gamma$  are orthogonal spatial coordinates) and easily integrated using the Jacobian of the transformation (see the Colab notebook [Spectral-element interpolation](#)). However, we can only use Lagrange polynomials when the dimensions of elements are independent of each other, such as in the canonical basis  $(\xi, \eta, \gamma)$ . That means elements must be rectangles (in 2D) or regular hexahedrons (in 3D) with all faces parallel to the planes formed by all the three axes of the reference system. However, when we transform them to another basis such as  $(x, y, z)$  or even  $(r, \theta, \phi)$ , they usually undergo distortions, and the coordinates lose their linear independence and become coupled. Therefore, we always apply interpolation in the canonical domain.

Although Lagrange polynomials work just fine, for performance reasons, in our implementation, we assemble a linear system of equations to fit a 3D polynomial to each spectral element on the standard basis in which all elements are identical. Once we have the coefficients, we can reuse them to interpolate any other element. In this paper, we call that approach *generic interpolation* (see the Colab notebook [Generic interpolation](#)). The shape functions (Komatitsch and Tromp, 1999, 2002a) are the map that transforms  $(\xi, \eta, \gamma)$  values from the standard basis to  $(x, y, z)$  values on another basis (the corresponding coordinate in the deformed spectral element). When the map is linear, the inversion is trivial, and for a given set of  $(x_i, y_i, z_i)$  values, we can use the inverse map to calculate the corresponding  $(\xi_i, \eta_i, \gamma_i)$  values. When the map is nonlinear, numerical optimization methods (such as Newton's method or other Householder's methods) can be used to

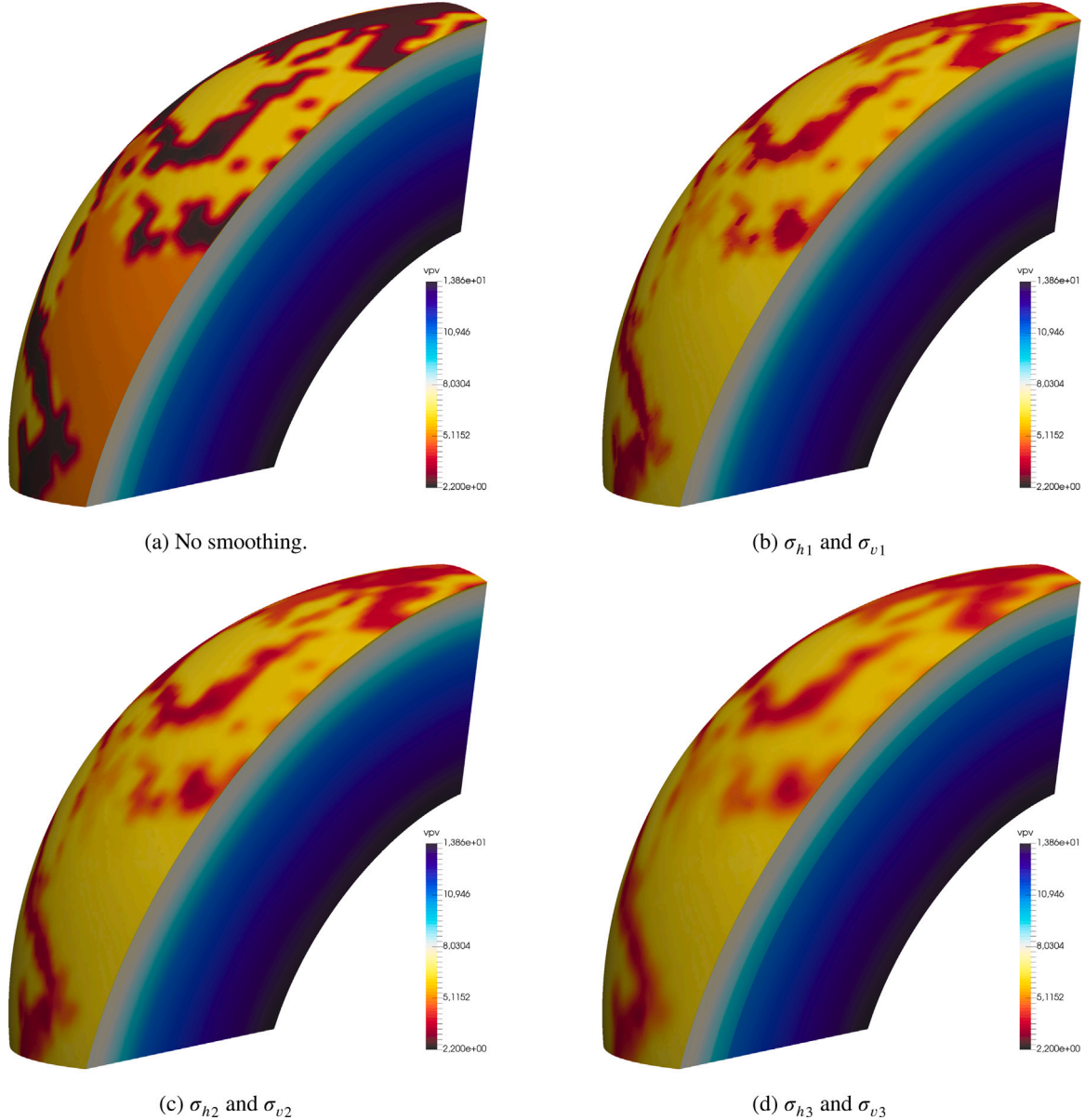


**Fig. 10.** S362ANI (Kustowski et al., 2008) with different degrees of smoothing (see Table 1 for the values of smoothing parameters). (a) Vertically-polarized compressional-wave velocities ( $V_{PV}$ ) without smoothing. (b)  $V_{PV}$  values smoothed using the horizontal and vertical standard deviations  $\sigma_{h1}$  and  $\sigma_{v1}$ , respectively. (c)  $V_{PV}$  values smoothed using the standard deviations  $\sigma_{h2}$  and  $\sigma_{v2}$ . (d)  $V_{PV}$  values smoothed using the standard deviations  $\sigma_{h3}$  and  $\sigma_{v3}$  preserving the 410 and 650 km discontinuities.

reverse the mapping (see the Colab notebook [Householder's methods](#)). Once we find  $(\xi_i, \eta_j, \gamma_i)$ , we can interpolate the values using either Lagrange polynomials or generic interpolation.

Because we define Lagrange polynomials for the whole space, in theory, they should also work outside a spectral element. However, when there are regions in which the Jacobian becomes singular, we cannot always carry out the inverse mapping from  $(x, y, z)$  to  $(\xi, \eta, \gamma)$ . To overcome this problem, one should always check which spectral element encloses the point we want to interpolate before inverting the mapping using the respective Jacobian. To check whether that condition is fulfilled, we need to fit 2D surfaces to each of six faces of an element (Fig. 11). In SPECFEM3D\_GLOBE, by default, each spectral element has 125 ( $5 \times 5 \times 5$ ) GLL grid points and 27 ( $3 \times 3 \times 3$ ) control, or anchor, nodes for the mapping. That leaves us with nine control nodes on each face. Thus, we need to fit quadratic surfaces  $P(x, y)$  in the

following form

$$\begin{aligned}
 P(x, y) = & \sum_{i=0}^2 \sum_{j=0}^2 a_{ij} x^i y^j = a_{00} \\
 & + a_{10} x + a_{01} y \\
 & + a_{11} x y + a_{20} x^2 + a_{02} y^2 \\
 & + a_{21} x^2 y + a_{12} x y^2 \\
 & + a_{22} x^2 y^2.
 \end{aligned} \tag{18}$$

Although the generic polynomial interpolation can handle a distorted grid, the accuracy of results may be affected depending on how uneven the nodes distribution is, potentially leading to surfaces with extreme curvatures. However, it is possible to mitigate the problem if we choose the correct orientation of each face. We should parametrize a

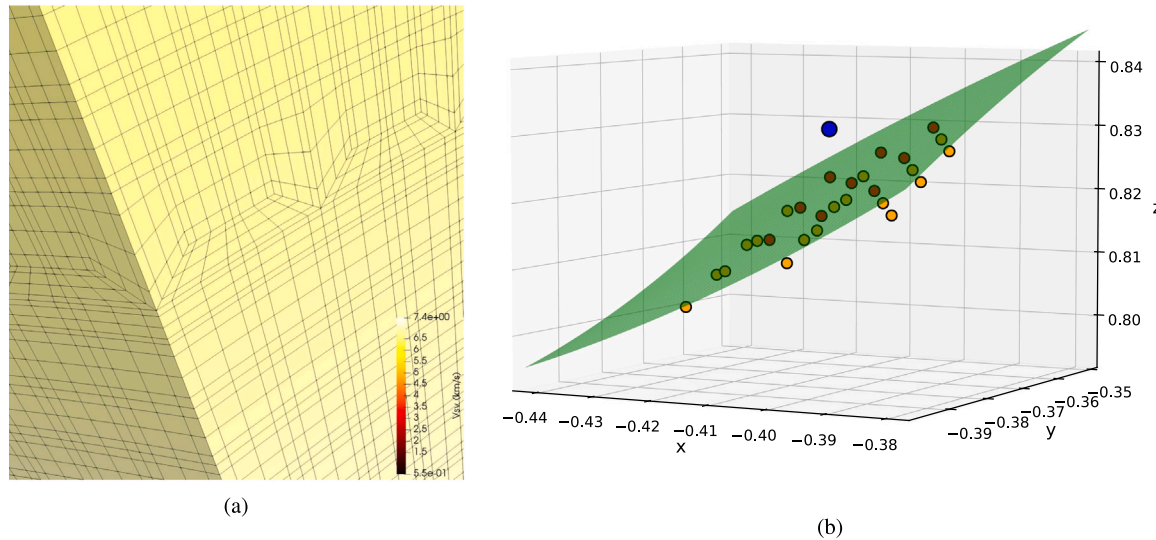


**Fig. 11.** (a) Global mesh for S362ANI showing all the internal points and connections focusing on the doubling layer in the middle of the lower mantle (Komatitsch and Tromp, 2002a). (b) Schematic representation of the 27 control nodes (red and orange) inside a spectral element in the doubling layer. The interpolation algorithm compares the relative position of a point (blue) to surfaces fitted to each of the six faces to check whether the point (blue) is inside or outside the element. The surface (green) fits the nine nodes (in red) at the upper face of the element (Eq. (18)). Note that spectral elements from doubling layers may impose challenges for interpolation. When fitting the surface to the face becomes numerically unstable, the algorithm resorts to alternative interpolation methods such as constrained interpolation (Eq. (19)).

face whose normal vector predominantly points the  $z$  direction in terms of  $(x, y)$ . On the other hand, if the face points mainly in the  $y$  direction, we should parametrize it as  $P(x, z)$ . Analogously, we should use  $P(y, z)$  for any surface primarily oriented in the  $x$  direction. Nevertheless, checking the orientation usually is not enough to guarantee the best fitting. In our implementation, we use a brute-force approach that consists of fitting surfaces for all three directions and picking the best one based on the norm of the coefficients, the mean surface curvature, and the residuals. When the algorithm fails to fit a surface (Eq. (18)) to the nine nodes, it automatically resorts to an alternative approach, which consists of fitting only the four corner nodes of the face using the following equation:

$$P(x, y) = a_{00} + a_{10}x + a_{01}y + a_{11}xy + a_{20}x^2 + a_{02}y^2. \quad (19)$$

Since there are infinitely many surfaces in the above form that contain all four points, a reasonable idea would be to choose the one with minimum curvature. By imposing that the quadratic terms are as small as possible using Lagrange multipliers, the two additional terms become zero when we have a regular grid, and we perfectly recover the bilinear interpolation. We call that approach *constrained interpolation* (see the Colab notebook [Constrained interpolation](#)).

For our particular case, we enhanced the method by including the central node of the face as well. We end up with five nodes to fit and six unknowns. Again, we avoid the underdetermination by imposing a minimum-curvature surface. The penalty for using a lower-degree polynomial is that, sometimes, when a face is trying to accommodate sharp topographic variations (such as the Himalayas), the simplified surface cannot represent all the complexity properly. When that occurs, we observe large residuals between the surface and some of the points in the face. To address such cases, we apply corrections to surfaces to reduce the residuals using a relatively simple yet robust interpolation scheme known as Inverse Distance Weighting (IDW). IDW is an interpolation method that works for any number of dimensions and with any data set distribution. In general, it does not provide a high-quality result. However, the simplicity, robustness, and flexibility of IDW make it useful for applications where we cannot apply other methods or when high accuracy is not needed. Besides, unlike the nearest-neighbor

algorithm, it provides a smooth interpolation. The corrections are calculated using all the 9 control nodes of each face, and no search radius is required. Using more sophisticated methods such as natural neighbor interpolation (Sibson, 1981) or kriging (Matheron, 1963) would likely lead to superior topographic corrections but also increase the algorithm complexity and the computational cost. These corrections are relevant for just a few spectral elements, and IDW provides enough accuracy to address such cases at a lower computational cost. It is worth noting that the goal of these corrections is to ensure that all points are properly assigned to their respective enclosing elements. Provided that the assignment is correct, extra accuracy in these corrections would not impact the model interpolation quality. For more details on IDW, see the corresponding Colab notebook [Inverse distance weighting](#).

## 6. Conclusion

We present SphGLLTools, a toolbox designed to facilitate easy visualization, processing, and analysis of large-scale tomographic models defined on spectral-element meshes by expanding them onto spherical harmonics while keeping the top 80 km as a block model. The SphGLLTools toolbox allows for easy and practical visualization of spectral-element models using either direct interpolation or the flexible expansion using spherical harmonics while taking advantage of GMT6 to create high-quality images. The additional routines in the toolbox operate on spectral-element meshes in parallel for interpolation, remeshing, and smoothing, which are useful for the adjoint tomography workflow that encompasses creating a new adjoint model and future studies using different resolution computational resources. We also lead the reader through a comprehensible yet intuitive explanation of the theory and concepts used by the routines in Colab notebooks available at <https://github.com/caiociardelli/sphgltools/tree/main/doc>.

The spherical harmonic expansion of spectral-element models significantly reduces the size of GLL models by several orders of magnitude and allows for a convenient way of analyzing, sharing, and exploring them on personal computers. As an example, as mentioned in Section 2, the original GLAD-M15 and GLAD-M25 models sampled on their corresponding GLL meshes occupy 47 GB of disk space each (including

model and mesh files). On the other hand, the expansions in B-splines & spherical harmonics of the whole mantle of GLAD-M15 and GLAD-M25 occupy only ~29 MB and ~55 MB, respectively. The high-resolution block crustal models of GLAD-M15 and GLAD-M25 down to 80 km depth occupy ~537 MB. In the future, we will implement spherical harmonic models directly in the numerical solver to run seismic wave simulations at different mesh resolutions and the number of processors, avoiding intermediate steps like mesh interpolation and model partitioning.

#### CRediT authorship contribution statement

**Caio Ciardelli:** Created the toolbox, Wrote the paper. **Ebru Bozdağ:** Supervised the study, Wrote the paper. **Daniel Peter:** Implemented spherical harmonic models into SPECFEM3D\_GLOBE, Revised the paper and the manual. **Suzan van der Lee:** Provided advice for the toolbox, Revised the paper and the Colab notebooks.

#### Declaration of competing interest

The authors declare that they have no known competing financial interests or personal relationships that could have appeared to influence the work reported in this paper.

#### Acknowledgments

We thank editor Dario Grana, Bernhard Schuberth, Carl Tape and an anonymous reviewer for constructive feedback which greatly improved the manuscript. We gratefully acknowledge the discussions with Jeroen Tromp on the spherical harmonic expansion of global tomographic models sampled on spectral-element meshes. CC thanks the São Paulo Research Foundation (FAPESP), Brazil (Grants: 2016/03120-5, 2018/04918-6, and 2018/04917-0) for providing financial support. EB is supported by the U.S. National Science Foundation under grant number EAR 1945565. This research was supported in part through the computational resources and staff contributions provided for the Quest high-performance computing facility at Northwestern University, which is jointly supported by the Office of the Provost, the Office for Research, and Northwestern University Information Technology. The authors also acknowledge the Texas Advanced Computing Center (TACC) at The University of Texas at Austin for providing computational resources on Frontera system (Stanzione et al., 2020) that have contributed to the research results reported within this paper through allocation EAR21003 ([www.tacc.utexas.edu](http://www.tacc.utexas.edu)). The SphGLLTools toolbox, including the documentation and the examples, is available at <https://github.com/caiociardelli/sphgltools.git>. The open source spectral-element software package SPECFEM3D\_GLOBE is freely available via the Computational Infrastructure for Geodynamics (CIG; [geodynamics.org](http://geodynamics.org)).

#### Appendix

Following Tarantola (2005), we use the logarithmic of the model parameters  $\ln [M(x)]$ , where  $x$  denotes the position. It follows that a perturbation is:

$$d\ln [M(x)] = \ln [M(x)] - \ln [M_{ref}(x)] = \ln \left[ \frac{M(x)}{M_{ref}(x)} \right], \quad (20)$$

where  $M(x)$  is the perturbed model, and  $M_{ref}(x)$  is the reference model. In our case,  $M_{ref}$  is the one-dimensional mean model  $M_{mean}$ . By mean model, we refer to the arithmetic mean of the three-dimensional model per depth. However, the above result is not balanced as the mean of the perturbations is close, but not exactly zero. To overcome that problem, we use instead:

$$d\ln [M(x)] = \ln \left[ \frac{M(x)}{M_{mean}(x)} \right] - \left\{ \ln \left[ \frac{M(x)}{M_{mean}(x)} \right] \right\}_{mean}. \quad (21)$$

But, with some manipulation of the right-hand side:

$$\begin{aligned} d\ln [M(x)] &= \ln [M(x)] - \ln [M_{mean}(x)] \\ &\quad - \left\{ \ln [M(x)] - \ln [M_{mean}(x)] \right\}_{mean} \\ &= \ln [M(x)] - \ln \left[ \overline{M_{mean}(x)} + \ln [M_{mean}(x)] \right] \\ &\quad - \frac{1}{N} \sum_{i=0}^N \ln [M_i(x)] \\ &= \ln [M(x)] - \frac{1}{N} \ln \left[ \prod_{i=0}^N M_i(x) \right]^{\frac{1}{N}} \\ &= \ln [M(x)] - \ln \left[ \prod_{i=0}^N M_i(x) \right]^{\frac{1}{N}} \\ &= \ln [M(x)] - \ln [M_{gmean}(x)] \\ &= \ln \left[ \frac{M}{M_{gmean}(x)} \right], \end{aligned} \quad (22)$$

where  $M_{gmean}$  is a one-dimensional geometric-mean model.

#### References

Afanasiev, M., Peter, D., Sager, K., Simutė, S., Ermert, L., Krischer, L., Fichtner, A., 2016. Foundations for a multiscale collaborative Earth model. *Geophys. J. Int.* 204 (1), 39–58. <http://dx.doi.org/10.1093/gji/ggv439>.

Ahlberg, J.H., Nilson, E.N., Walsh, J.L., 1967. *The theory of splines and their applications*. Math. Sci. Eng.

Ahrens, J., Geveci, B., Law, C., 2005. Paraview: An end-user tool for large data visualization. In: *The Visualization Handbook*, Vol. 717 no. 8. Elsevier Oxford, UK, <http://dx.doi.org/10.1016/B978-012387582-2/50038-1>.

Aratijo, R.R., Gross, L., de Souza, S.X., 2021. Boosting memory access locality of the spectral element method with Hilbert space-filling curves. *Comput. Geosci.* 157, 104938. <http://dx.doi.org/10.1016/j.cageo.2021.104938>.

Balmino, G., Moynot, B., Vales, N., 1982. Gravity field model of mars in spherical harmonics up to degree and order eighteen. *J. Geophys. Res. Solid Earth* 87 (B12), 9735–9746. <http://dx.doi.org/10.1029/JB087iB12p09735>.

Bassin, C., Laske, G., Masters, G., 2000. The current limits of resolution for surface wave tomography in north america. In: *EOS*, Vol. F897. p. 81.

Berljajac, J.M., Mishra, P.K., Slak, J., Kosec, G., 2021. RBF-FD Analysis of 2D time-domain acoustic wave propagation in heterogeneous media. *Comput. Geosci.* 153, 104796. <http://dx.doi.org/10.1016/j.cageo.2021.104796>.

Boehm, C., Hanzich, M., de la Puente, J., Fichtner, A., 2016. Wavefield compression for adjoint methods in full-waveform inversion. *Geophysics* 81 (6), R385–R397. <http://dx.doi.org/10.1190/geo2015-0653.1>.

Boschi, L., Dziewonski, A., 2000. Whole earth tomography from delay times of P, Pcp and PKP phases: Lateral heterogeneities in the outer core and radial anisotropy in the mantle? *J. Geophys. Res.* 105 (B6), 13675–13696.

Boschi, L., Ekström, G., 2002. New images of the earth's upper mantle from measurements of surface wave phase velocity anomalies. *J. Geophys. Res.* 107 (B4), 2059.

Bozdağ, E., Peter, D., Lefebvre, M., Komatsitsch, D., Tromp, J., Hill, J., Podhorszki, N., Pugmire, D., 2016. Global adjoint tomography: first-generation model. *Geophys. J. Int.* 207 (3), 1739–1766. <http://dx.doi.org/10.1093/gji/ggw356>.

Bozdağ, E., Trampert, J., 2008. On crustal corrections in surface wave tomography. *Geophys. J. Int.* 172 (3), 1066–1082. <http://dx.doi.org/10.1111/j.1365-246X.2007.03690.x>.

Burggraf, D., 2015. OGC KML 2.3, Version 1.0.. URL <http://docs.opengeospatial.org/is/12-007r2/12-007r2.html>.

Capdeville, Y., Chaljub, E., Montagner, J.P., 2003. Coupling the spectral element method with a modal solution for elastic wave propagation in global earth models. *Geophys. J. Int.* 152 (1), 34–67. <http://dx.doi.org/10.1046/j.1365-246X.2003.01808.x>.

Capdeville, Y., Marigo, J.-J., 2007. Second order homogenization of the elastic wave equation for non-periodic layered media. *Geophys. J. Int.* 823–838. <http://dx.doi.org/10.1111/j.1365-246X.2007.03462.x>.

Carle, H., Harrison, C., 1982. A problem in representing the core magnetic field of the earth using spherical harmonics. *Geophys. Res. Lett.* 9 (4), 265–268. <http://dx.doi.org/10.1029/GL009i004p00265>.

Chaljub, E., 2000. *Modélisation numérique de la propagation d'ondes sismiques en géométrie sphérique: application à la sismologie globale*. (Ph.D. thesis). Université Paris-Diderot-Paris VII.

Chaljub, E., Capdeville, Y., Vilotte, J.-P., 2003. Solving elastodynamics in a fluid-solid heterogeneous sphere: A parallel spectral element approximation on non-conforming grids. *J. Comput. Phys.* 187 (2), 457–491. [http://dx.doi.org/10.1016/S0021-9991\(03\)00119-0](http://dx.doi.org/10.1016/S0021-9991(03)00119-0).

Chang, S.-J., Ferreira, A.M., Ritsema, J., van Heijst, H.J., Woodhouse, J.H., 2015. Joint inversion for global isotropic and radially anisotropic mantle structure including crustal thickness perturbations. *J. Geophys. Res. Solid Earth* 120 (6), 4278–4300. <http://dx.doi.org/10.1002/2014JB011824>.

Chang, S.-J., Ferreira, A.M.G., Ritsema, J., van Heijst, H.J., Woodhouse, J.H., 2014. Global radially anisotropic mantle structure from multiple datasets: A review, current challenges, and outlook. *Tectonophysics* 617, 1–19. <http://dx.doi.org/10.1016/j.tecto.2014.01.033>.

Chen, M., Huang, H., Yao, H., van der Hilst, R., Niu, F., 2014. Low wave speed zones in the crust beneath SE Tibet revealed by ambient noise adjoint tomography. *Geophys. Res. Lett.* 41 (2), 334–340. <http://dx.doi.org/10.1002/2013GL058476>.

Chevrot, S., Montagner, J., Snieder, R., 1998. The spectrum of tomographic earth models. *Geophys. J. Int.* 133 (3), 783–788. <http://dx.doi.org/10.1046/j.1365-246X.1998.00542.x>.

Dahlen, F., Tromp, J., 1998. *Theoretical Global Seismology*. Princeton University Press.

DeMets, C., Gordon, R.G., Argus, D.F., 2010. Geologically current plate motions. *Geophys. J. Int.* 181 (1), 1–80. <http://dx.doi.org/10.1111/j.1365-246X.2009.04491.x>.

Dong, X., Yang, D., Niu, F., Liu, S., Tong, P., 2021. Adjoint traveltimes tomography unravels a scenario of horizontal mantle flow beneath the north China craton. *Sci. Rep.* 11 (1), 1–11. <http://dx.doi.org/10.1038/s41598-021-92048-8>.

Dziewonski, A.M., Anderson, D.L., 1981. Preliminary reference earth model. *Phys. Earth Planet. Inter.* 25 (4), 297–356. [http://dx.doi.org/10.1016/0031-9201\(81\)90046-7](http://dx.doi.org/10.1016/0031-9201(81)90046-7).

Dziewonski, A.M., Hager, B.H., O'Connell, R.J., 1977. Large-scale heterogeneities in the lower mantle. *J. Geophys. Res.* 82 (2), 239–255. <http://dx.doi.org/10.1029/JB082i002p00239>.

Ekström, G., Dziewonski, A.M., 1998. The unique anisotropy of the Pacific upper mantle. *Nature* 394 (6689), 168–172. <http://dx.doi.org/10.1038/28148>.

Ferreira, A., Woodhouse, J., Visser, K., Trampert, J., 2010. On the robustness of global radially anisotropic surface wave tomography. *J. Geophys. Res. Solid Earth* 115 (B4). <http://dx.doi.org/10.1029/2009JB006716>.

Fichtner, A., Bunge, H.P., Igel, H., 2006a. The adjoint method in seismology-I. Theory. *Phys. Earth Planet. Inter.* 157 (1), 86–104. <http://dx.doi.org/10.1016/j.pepi.2006.03.016>.

Fichtner, A., Bunge, H.P., Igel, H., 2006b. The adjoint method in seismology-II. Applications: Traveltimes and sensitivity functionals. *Phys. Earth Planet. Inter.* 157 (1), 105–123. <http://dx.doi.org/10.1016/j.pepi.2006.03.018>.

Fichtner, A., Kennett, B.L.N., Igel, H., Bunge, H.-P., 2009. Full seismic waveform tomography for upper-mantle structure in the australasian region using adjoint methods. *Geophys. J. Int.* 179 (3), 1703–1725. <http://dx.doi.org/10.1111/j.1365-246X.2009.04368.x>.

Fichtner, A., Saygin, E., Taymaz, T., Cupillard, P., Capdeville, Y., Trampert, J., 2013. The deep structure of the north Anatolian fault zone. *Earth Planet. Sci. Lett.* 373, 109–117. <http://dx.doi.org/10.1016/j.epsl.2013.04.027>.

French, S.W., Romanowicz, B.A., 2014. Whole-mantle radially anisotropic shear velocity structure from spectral-element waveform tomography. *Geophys. J. Int.* 199 (3), 1303–1327. <http://dx.doi.org/10.1093/gji/ggu334>.

Gao, L., Keyes, D., 2019. Combining finite element and finite difference methods for isotropic elastic wave simulations in an energy-conserving manner. *J. Comput. Phys.* 378, 665–685. <http://dx.doi.org/10.1016/j.jcp.2018.11.031>.

Giardini, D., Li, X.-D., Woodhouse, J.H., 1988. Splitting functions of long-period normal modes of the earth. *J. Geophys. Res.* 93, 13716–13742.

Gu, Y.J., Dziewonski, A.M., Su, W., Ekström, G., 2001. Models of the mantle shear velocity and discontinuities in the pattern of lateral heterogeneities. *J. Geophys. Res. Solid Earth* 106 (B6), 11169–11199. <http://dx.doi.org/10.1029/2001JB000340>.

Hosseini, K., Matthews, K.J., Sigloch, K., Shephard, G.E., Domeier, M., Tsekhnistrenko, M., 2018. SubMachine: Web-based tools for exploring seismic tomography and other models of earth's deep interior. *Geochemistry, Geophysics, Geosystems* 19 (5), 1464–1483. <http://dx.doi.org/10.1029/2018GC007431>.

Hutko, A.R., Bahavar, M., Trabant, C., Weekly, R.T., Fossen, M.V., Ahern, T., 2017. Data products at the IRIS-DMC: Growth and usage. *Seismol. Res. Lett.* 88 (3), 892–903. <http://dx.doi.org/10.1785/0220160190>.

Kissling, E., Husen, S., Haslinger, F., 2001. Model parametrization in seismic tomography: a choice of consequence for the solution quality. *Phys. Earth Planet. Inter.* 123 (2–4), 89–101. [http://dx.doi.org/10.1016/S0031-9201\(00\)00203-X](http://dx.doi.org/10.1016/S0031-9201(00)00203-X).

Komatitsch, D., Tromp, J., 1999. Introduction to the spectral element method for three-dimensional seismic wave propagation. *Geophys. J. Int.* 139 (3), 806–822. <http://dx.doi.org/10.1046/j.1365-246X.1999.00967.x>.

Komatitsch, D., Tromp, J., 2002a. Spectral-element simulations of global seismic wave propagation—I. validation. *Geophys. J. Int.* 149 (2), 390–412. <http://dx.doi.org/10.1046/j.1365-246X.2002.01653.x>.

Komatitsch, D., Tromp, J., 2002b. Spectral-element simulations of global seismic wave propagation—II. three-dimensional models, oceans, rotation and self-gravitation. *Geophys. J. Int.* 150 (1), 303–318. <http://dx.doi.org/10.1046/j.1365-246X.2002.01716.x>.

Komatitsch, D., Vilotte, J.-P., 1998. The spectral element method: an efficient tool to simulate the seismic response of 2D and 3D geological structures. *Bull. Seismol. Soc. Am.* 88 (2), 368–392, URL <https://pubs.geoscienceworld.org/ssa/bssa/article-pdf/88/2/368/2709303/BSSA0880020368.pdf>.

Komatitsch, D., Xie, Z., Bozdağ, E., Sales de Andrade, E., Peter, D., Liu, Q., Tromp, J., 2016. Anelastic sensitivity kernels with parsimonious storage for adjoint tomography and full waveform inversion. *Geophys. J. Int.* 206 (3), 1467–1478. <http://dx.doi.org/10.1093/gji/ggw224>.

Koranne, S., 2011. Hierarchical data format 5: HDF5. In: *Handbook of Open Source Tools*. Springer, pp. 191–200.

Kustowski, B., Ekström, G., Dziewoński, A., 2008. Anisotropic shear-wave velocity structure of the earth's mantle: A global model. *J. Geophys. Res. Solid Earth* 113 (B6). <http://dx.doi.org/10.1029/2007JB005169>.

Laske, G., Masters, G., Ma, Z., Pasyanos, M., 2012. CRUST1.0: An updated global model of Earth's crust. *Geophys. Res. Abs.* 14, 3743. <http://dx.doi.org/10.17611/DP/emccrust10>.

Lebedev, S., Nolet, G., Meier, T., van der Hilst, R.D.G., 2005. Automated multimode inversion of surface and S waveforms. *Geophys. J. Int.* 162, 951–964.

Lei, W., Ruan, Y., Bozdağ, E., Peter, D., Lefebvre, M., Komatitsch, D., Tromp, J., Hill, J., Podhorszki, N., Pugmire, D., 2020. Global adjoint tomography-model GLAD-M25. *Geophys. J. Int.* 223 (1), 1–21. <http://dx.doi.org/10.1093/gji/ggaa253>.

Lekić, V., Romanowicz, B., 2011. Inferring upper-mantle structure by full waveform tomography with the spectral element method. *Geophys. J. Int.* 185 (2), 799–831. <http://dx.doi.org/10.1111/j.1365-246X.2011.04969.x>.

Li, X.-D., Romanowicz, B., 1996. Global mantle shear velocity model developed using nonlinear asymptotic coupling theory. *J. Geophys. Res. Solid Earth* 101 (B10), 22245–22272. <http://dx.doi.org/10.1029/96JB01306>.

Liu, Q., Logan, J., Tian, Y., Abbasi, H., Podhorszki, N., Choi, J.Y., Klasky, S., Tchoua, R., Lofstead, J., Oldfield, R., et al., 2014. Hello ADIOS: the challenges and lessons of developing leadership class I/O frameworks. *Concurr. Comput.: Pract. Exper.* 26 (7), 1453–1473. <http://dx.doi.org/10.1002/cpe.3125>.

Marquering, H., Dahlen, F.A., Nolet, G., 1999. Three-dimensional sensitivity kernels for finite-frequency traveltimes: The banana-doughnut paradox. *Geophys. J. Int.* 137 (3), 805–815. <http://dx.doi.org/10.1046/j.1365-246X.1999.00837.x>.

Matheron, G., 1963. Principles of geostatistics. *Econ. Geol.* 58 (8), 1246–1266. <http://dx.doi.org/10.2131/gcongeo.58.8.1246>.

Mégnin, C., Romanowicz, B., 2000. The three-dimensional shear velocity structure of the mantle from the inversion of body, surface and higher-mode waveforms. *Geophys. J. Int.* 143 (3), 709–728. <http://dx.doi.org/10.1046/j.1365-246X.2000.00298.x>.

Moczo, P., Kristek, J., Galis, M., Pazak, P., Balazovjech, M., 2007. The finite-difference and finite-element modeling of seismic wave propagation and earthquake motion. *Acta Phys. Slovaca* 57 (2), URL <https://inis.iaea.org/search/searchsinglerecord.aspx?recordsFor=SingleRecord&RN=47049418>.

Montelli, R., Nolet, G., Dahlen, F.A., Masters, G., Engdahl, E.R., Hung, S.-H., 2004. Finite-frequency tomography reveals a variety of plumes in the mantle. *Science* 303 (5656), 338–343. <http://dx.doi.org/10.1126/science.1092485>.

Moulik, P., Ekström, G., 2014. An anisotropic shear velocity model of the Earth's mantle using normal modes, body waves, surface waves and long-period waveforms. *Geophys. J. Int.* 199 (3), 1713–1738. <http://dx.doi.org/10.1093/gji/ggu356>.

Pan, W., Innanen, K.A., Wang, Y., 2020. SeisElastic2D: An open-source package for multiparameter full-waveform inversion in isotropic-, anisotropic-and viscoelastic media. *Comput. Geosci.* 145, 104586. <http://dx.doi.org/10.1016/j.cageo.2020.104586>.

Plessix, R.-E., 2006. A review of the adjoint-state method for computing the gradient of a functional with geophysical applications. *Geophys. J. Int.* 167 (2), 495–503. <http://dx.doi.org/10.1111/j.1365-246X.2006.02978.x>.

Postpischl, L., Danecek, P., Morelli, A., Pondrelli, S., 2011. Standardization of seismic tomographic models and earthquake focal mechanisms data sets based on web technologies, visualization with keyhole markup language. *Comput. Geosci.* 37 (1), 47–56. <http://dx.doi.org/10.1016/j.cageo.2010.05.006>.

Prautzsch, H., Boehm, W., Paluszny, M., 2002. BÉZier and B-Spline Techniques, Vol. 6. Springer, <https://link.springer.com/book/10.1007%2F978-3-662-04919-8>.

QGIS Development Team, 2009. QGIS Geographic Information System. Open Source Geospatial Foundation, URL <http://qgis.osgeo.org>.

Ritsema, J., Deuss, A.A., Van Heijst, H., Woodhouse, J., 2011. S40RTS: a degree-40 shear-velocity model for the mantle from new Rayleigh wave dispersion, teleseismic traveltimes and normal-mode splitting function measurements. *Geophys. J. Int.* 184 (3), 1223–1236. <http://dx.doi.org/10.1111/j.1365-246X.2010.04884.x>.

Ritsema, J., Van Heijst, H.J., Woodhouse, J.H., 1999. Complex shear wave velocity structure imaged beneath Africa and Iceland. *Science* 286 (5446), 1925–1928. <http://dx.doi.org/10.1126/science.286.5446.1925>.

Roithmayr, C.M., 2004. Contributions of spherical harmonics to magnetic and gravitational fields. URL <https://ntrs.nasa.gov/citations/20040047194>.

Salomon, D., 2006. *Data Compression: The Complete Reference*. Springer Science & Business Media.

Schmidt, M., Fabert, O., Shum, C., 2005. On the estimation of a multi-resolution representation of the gravity field based on spherical harmonics and wavelets. *J. Geodyn.* 39 (5), 512–526. <http://dx.doi.org/10.1016/j.jog.2005.04.007>.

Schroeder, W., Martin, K., Lorenzen, B., 2006. *The Visualization Toolkit*, 4th Edn. Kitware, New York.

Schuberth, B., 2003. The spectral-element method for seismic wave propagation: theory, implementation and comparison to finite difference methods (Master's Thesis), Ludwig-Maximilians-Universität MÜNchen, Unpublished.

Sibson, R., 1981. A brief description of natural neighbour interpolation. *Interpret. Multivar. Data*.

Snieder, R., Beckers, J., Neele, F., 1991. The effect of small-scale structure on normal mode frequencies and global inversions. *J. Geophys. Res.* 96, 501–515.

Spetzler, J., Trampert, J., Snieder, R., 2001. Are we exceeding the limits of the great circle approximation in global surface wave tomography? *Geophys. Res. Lett.* 28 (12), 2341–2344. <http://dx.doi.org/10.1029/2000GL012691>.

Stanzione, D., West, J., Evans, R.T., Minyard, T., Ghattas, O., Panda, D.K., 2020. Frontera: the evolution of leadership computing at the national science foundation. In: Practice and Experience in Advanced Research Computing (PEARC '20), July 26–30, 2020, Portland, OR, USA. ACM, New York, NY, USA, 11 pages <http://dx.doi.org/10.1145/3311790.3396656>.

Tape, C., Liu, Q., Maggi, A., Tromp, J., 2009. Adjoint tomography of the southern California crust. *Science* 325 (5943), 988–992, URL <https://science.sciencemag.org/content/325/5943/988>.

Tarantola, A., 1984. Inversion of seismic reflection data in the acoustic approximation. *Geophysics* 49 (8), 1259–1266. <http://dx.doi.org/10.1190/1.1441754>.

Tarantola, A., 2005. Inverse Problem Theory and Methods for Model Parameter Estimation. SIAM, <http://dx.doi.org/10.1137/1.9780898717921>.

Teodor, D., Comina, C., Socco, L., Anjom, F.K., Virieux, J., Brossier, R., Trinh, P., 2019. Elastic full waveform inversion tests for shallow targets reconstruction from surface waves analysis based initial models. In: 81st EAGE Conference and Exhibition 2019. 2019, (1), European Association of Geoscientists & Engineers, pp. 1–5. <http://dx.doi.org/10.3997/2214-4609.201900976>.

Trabant, C., Hutko, A.R., Bahavar, M., Karstens, R., Ahern, T., Aster, R., 2012. Data products at the IRIS DMC: Stepping stones for research and other applications. *Seismol. Res. Lett.* 83 (5), 846–854. <http://dx.doi.org/10.1785/0220120032>.

Trinh, P.-T., Brossier, R., Métivier, L., Tavard, L., Virieux, J., Wellington, P., 2017. Efficient 3D elastic FWI using a spectral-element method on cartesian-based mesh. In: SEG Technical Program Expanded Abstracts 2017. Society of Exploration Geophysicists, pp. 1533–1538. <http://dx.doi.org/10.1190/segam2017-17587770.1>.

Tromp, J., Komatitsch, D., Hjörleifsdóttir, V., Liu, Q., Zhu, H., Peter, D., Bozdag, E., McRitchie, D., Friberg, P., Trabant, C., Hutko, A., 2010. Near real-time simulations of global CMT earthquakes. *Geophys. J. Int.* 183 (1), 381–389. <http://dx.doi.org/10.1111/j.1365-246X.2010.04734.x>.

Tromp, J., Tape, C., Liu, Q., 2005. Seismic tomography, adjoint methods, time reversal and banana-doughnut kernels. *Geophys. J. Int.* 160 (1), 195–216. <http://dx.doi.org/10.1111/j.1365-246X.2004.02453.x>.

Unidata, 2016. Network Common Data Form (netCDF). UCAR/Unidata Program Center, <http://dx.doi.org/10.5065/D6H70CW6>.

Wang, Z., Dahlen, F., 1995a. Spherical-spline parameterization of three-dimensional earth models. *Geophys. Res. Lett.* 22 (22), 3099–3102. <http://dx.doi.org/10.1029/95GL03080>.

Wang, Z., Dahlen, F.A., 1995b. Validity of surface-wave ray theory on a laterally heterogeneous earth. *Geophys. J. Int.* 123 (3), 757–773. <http://dx.doi.org/10.1111/j.1365-246X.1995.tb06888.x>.

Wang, K., Yang, Y., Basini, P., Tong, P., Tape, C., Liu, Q., 2018. Refined crustal and uppermost mantle structure of southern California by ambient noise adjoint tomography. *Geophys. J. Int.* 215 (2), 844–863. <http://dx.doi.org/10.1093/gji/ggy312>.

Wessel, P., Luis, J., Uieda, L., Scharroo, R., Wobbe, F., Smith, W., Tian, D., 2019. The generic mapping tools version 6. *Geochemistry, Geophysics, Geosystems* 20 (11), 5556–5564. <http://dx.doi.org/10.1029/2019GC008515>.

Woodhouse, J.H., Girmus, T.P., 1982. Surface waves and free oscillations in a regionalized earth model. *Geophys. J. Int.* 68 (3), 653–673. <http://dx.doi.org/10.1111/j.1365-246X.1982.tb04921.x>.

Yamagishi, Y., Nakanishi, A., Miura, S., Kodaira, S., Sakaguchi, H., 2018. Development of a database and visualization system integrating various models of seismic velocity structure and subducting plate geometry around Japan. *Prog. Earth Planet. Sci.* 5 (1), 1–9. <http://dx.doi.org/10.1186/s40645-018-0207-4>.

Zhou, H.W., 1996. A high resolution P wave model of the top 1200 km of the mantle. *J. Geophys. Res.* 101, 27791–27810.

Zhu, H., Bozdağ, E., Peter, D., Tromp, J., 2012. Structure of the European upper mantle revealed by adjoint tomography. *Nat. Geosci.* 5 (7), 493–498. <http://dx.doi.org/10.1038/ngeo1501>.

Zhu, H., Bozdağ, E., Tromp, J., 2015. Seismic structure of the European upper mantle based on adjoint tomography. *Geophys. J. Int.* 201 (1), 18–52. <http://dx.doi.org/10.1093/gji/ggu492>.